Galaxy and Mass Assembly (GAMA): *ugriz* galaxy luminosity functions

J. Loveday,[1]⋆ P. Norberg,[2,3] I. K. Baldry,[4] S. P. Driver,[5,6] A. M. Hopkins,[7]
J. A. Peacock,[2] S. P. Bamford,[8] J. Liske,[9] J. Bland-Hawthorn,[10] S. Brough,[7]
M. J. I. Brown,[11] E. Cameron,[12] C. J. Conselice,[8] S. M. Croom,[10] C. S. Frenk,[3]
M. Gunawardhana,[10] D. T. Hill,[5] D. H. Jones,[11] L. S. Kelvin,[5] K. Kuijken,[13]
R. C. Nichol,[14] H. R. Parkinson,[2] S. Phillipps,[15] K. A. Pimbblet,[11] C. C. Popescu,[16]
M. Prescott,[4] A. S. G. Robotham,[5] R. G. Sharp,[17] W. J. Sutherland,[18] E. N. Taylor,[10]
D. Thomas,[14] R. J. Tuffs,[19] E. van Kampen[9] and D. Wijesinghe[10]

[1]*Astronomy Centre, University of Sussex, Falmer, Brighton BN1 9QH*
[2]*Institute for Astronomy, University of Edinburgh, Royal Observatory, Blackford Hill, Edinburgh EH9 3HJ*
[3]*Department of Physics, Institute for Computational Cosmology, Durham University, South Road, Durham DH1 3LE*
[4]*Astrophysics Research Institute, Liverpool John Moores University, Twelve Quays House, Egerton Wharf, Birkenhead CH41 1LD*
[5]*School of Physics & Astronomy, University of St Andrews, North Haugh, St Andrews KY16 9SS*
[6]*International Centre for Radio Astronomy Research (ICRAR), The University of Western Australia, 35 Stirling Highway, Crawley, WA 6009, Australia*
[7]*Australian Astronomical Observatory, PO Box 296, Epping, NSW 1710, Australia*
[8]*Centre for Astronomy and Particle Theory, University of Nottingham, University Park, Nottingham NG7 2RD*
[9]*European Southern Observatory, Karl-Schwarzschild-Strasse 2, 85748 Garching, Germany*
[10]*Sydney Institute for Astronomy, School of Physics, University of Sydney, NSW 2006, Australia*
[11]*School of Physics, Monash University, Clayton, VIC 3800, Australia*
[12]*Department of Physics, Swiss Federal Institute of Technology (ETH-Zürich), 8093 Zürich, Switzerland*
[13]*Leiden University, PO Box 9500, 2300 RA Leiden, the Netherlands*
[14]*Institute of Cosmology and Gravitation (ICG), University of Portsmouth, Dennis Sciama Building, Burnaby Road, Portsmouth PO1 3FX*
[15]*Astrophysics Group, H. H. Wills Physics Laboratory, University of Bristol, Tyndall Avenue, Bristol BS8 1TL*
[16]*Jeremiah Horrocks Institute, University of Central Lancashire, Preston PR1 2HE*
[17]*Research School of Astronomy & Astrophysics, The Australian National University, Cotter Road, Weston Creek, ACT 2611, Australia*
[18]*Astronomy Unit, Queen Mary University London, Mile End Road, London E1 4NS*
[19]*Max Planck Institute for Nuclear Physics (MPIK), Saupfercheckweg 1, 69117 Heidelberg, Germany*

ABSTRACT

Galaxy and Mass Assembly (GAMA) is a project to study galaxy formation and evolution, combining imaging data from ultraviolet to radio with spectroscopic data from the AAOmega spectrograph on the Anglo-Australian Telescope. Using data from Phase 1 of GAMA, taken over three observing seasons, and correcting for various minor sources of incompleteness, we calculate galaxy luminosity functions (LFs) and their evolution in the *ugriz* passbands.

At low redshift, $z < 0.1$, we find that blue galaxies, defined according to a magnitude-dependent but non-evolving colour cut, are reasonably well fitted over a range of more than 10 magnitudes by simple Schechter functions in all bands. Red galaxies, and the combined blue plus red sample, require double power-law Schechter functions to fit a dip in their LF faintwards of the characteristic magnitude M^* before a steepening faint end. This upturn is at least partly due to dust-reddened disc galaxies.

We measure the evolution of the galaxy LF over the redshift range $0.002 < z < 0.5$ both by using a parametric fit and by measuring binned LFs in redshift slices. The characteristic luminosity L^* is found to increase with redshift in all bands, with red galaxies showing

⋆E-mail: J.Loveday@sussex.ac.uk

stronger luminosity evolution than blue galaxies. The comoving number density of blue galaxies increases with redshift, while that of red galaxies decreases, consistent with prevailing movement from blue cloud to red sequence. As well as being more numerous at higher redshift, blue galaxies also dominate the overall luminosity density beyond redshifts $z \simeq 0.2$. At lower redshifts, the luminosity density is dominated by red galaxies in the *riz* bands, and by blue galaxies in *u* and *g*.

Key words: galaxies: evolution – galaxies: luminosity function, mass function – galaxies: statistics.

1 INTRODUCTION

Measurements of the galaxy luminosity function (LF) and its evolution provide important constraints on theories of galaxy formation and evolution (see e.g. Benson et al. 2003). It is currently believed that galaxies formed hierarchically from the merger of subclumps. Looking back in time with increasing redshift, the star formation rate appears to peak at redshift $z \simeq 1$, above which it plateaus and slowly declines towards $z \simeq 6$ (Cole et al. 2000; Hopkins 2004; Hopkins & Beacom 2006; Yuksel et al. 2008; Kistler et al. 2009). Since $z \simeq 1$, galaxies are thought to have evolved mostly passively as their stellar population age, with occasional activity triggered by accretion and interactions with other galaxies. Noeske et al. (2007) have suggested that the first major burst of star formation is delayed to later times for low-mass galaxies, contributing to the downsizing phenomenon.

There has long been a discrepancy between the measured number density of low-luminosity galaxies (the 'faint end' of the LF) and predictions from cold dark matter hierarchical simulations, in the sense that fewer low-luminosity galaxies than predicted by most models are observed (Trentham & Tully 2002). Of course, interpretation of these simulation results is subject to uncertainties in the baryon physics. In particular, more effective feedback in low-mass haloes might act to suppress the faint end of the LF. However, it is also possible that many surveys have underestimated the number of dwarf galaxies due to the correlation between luminosity and surface brightness which makes them hard to detect (Driver 1999; Cross & Driver 2002; Cameron & Driver 2007, 2009). Geller et al. (2011) have recently demonstrated that the LF faint-end slope steepens with decreasing surface brightness.

Galaxy LFs have previously been measured in the *ugriz* bands from the Sloan Digital Sky Survey (SDSS, York et al. 2000) by Blanton et al. (2003b), Loveday (2004), Blanton et al. (2005b), Montero-Dorta & Prada (2009) and Hill et al. (2010). Blanton et al. (2003b) analysed a sample of 147 986 galaxies, roughly equivalent to the SDSS Data Release 1 (DR1, Abazajian et al. 2003). They fit the LF with a series of overlapping Gaussian functions, allowing the amplitude of each Gaussian to vary, along with two parameters Q and P describing, respectively, luminosity and density evolution. They maximized the joint likelihood of absolute magnitude and redshift, rather than the likelihood of absolute magnitude, given redshift, making this estimator more sensitive to evolution, as well as to density fluctuations due to large-scale structure. They found luminosity densities at $z = 0.1$ to increase systematically with effective wavelength of survey band, and for luminosity evolution to decline systematically with wavelength. Allowing for LF evolution enabled reconciliation of previously discrepant luminosity densities

obtained from SDSS commissioning data (Blanton et al. 2001) and the Two-degree Field Galaxy Redshift Survey (Folkes et al. 1999; Norberg et al. 2002).

Loveday (2004) measured the *r*-band LF in redshift slices from the SDSS DR1 and found that the comoving number density of galaxies brighter than $M_r - 5 \log h = -21.5$ mag was a factor of $\simeq 3$ higher at redshift $z = 0.3$ than today, due to luminosity and/or density evolution.

Blanton et al. (2005b) focused on the faint end of the LF of low-redshift galaxies from the SDSS DR2 (Abazajian et al. 2004), and found that a double-power-law Schechter function was required to fit an upturn in the LF at $M_r - 5 \log h \gtrsim -18$ mag with faint-end slope $\alpha_2 \simeq -1.5$ after correcting for low surface brightness incompleteness.

Montero-Dorta & Prada (2009) have analysed the SDSS DR6 (Adelman-McCarthy et al. 2008) which is roughly five times larger than the sample analysed by Blanton et al. (2003b). Their results are generally consistent with those of Blanton et al., although they do point out a bright-end excess above Schechter function fits, particularly in the *u* and *g* bands, due primarily to active galactic nuclei (AGNs). A bright-end excess above a best-fitting Schechter function has also been observed in near-infrared (near-IR) passbands by Jones et al. (2006).

Hill et al. (2010) analysed combined data sets from the Millennium Galaxy Catalogue (Liske et al. 2003), SDSS and UKIDSS Large Area Survey (Lawrence et al. 2007) over a common volume of $\simeq 71\,000\,h^{-3}$ Mpc^3 within redshift $z = 0.1$ to obtain LFs in the *ugrizYJHK* bands. They found that LFs in all bands were reasonably well fitted by Schechter functions, apart from tentative upturns at the faint ends of the *i*- and *z*-band LFs. Hill et al. provided the first homogeneous measurement of the luminosity density (LD) over the optical–near-IR regimes, finding a smooth spectral energy distribution (SED).

Here we present an estimate of *ugriz* galaxy LFs from the Galaxy and Mass Assembly (GAMA, Driver et al. 2009, 2011) survey. GAMA provides an ideal sample with which to constrain the galaxy LF at low to moderate redshifts due to its combination of moderately deep spectroscopic magnitude limit ($r < 19.4$ or $r < 19.8$) and wide-area sky coverage (three 4×12 deg^2 regions).

We describe the input galaxy sample and incompleteness, velocity and *K*-corrections in Section 2. Our LF-estimation procedure is described in Section 3 and tested using simulations in Appendix A. We present our results and a discussion of luminosity and density evolution in Section 4, with our conclusions summarized in Section 5.

Unless otherwise stated, we assume a Hubble constant of $H_0 = 100\,h$ km s^{-1} Mpc^{-1} and an $\Omega_M = 0.3$, $\Omega_\Lambda = 0.7$ cosmology in calculating distances, comoving volumes and luminosities.

2 DATA AND OBSERVATIONS

2.1 Input catalogue

The input catalogue for GAMA is described in detail by Baldry et al. (2010). In brief, it consists of three 4×12 deg^2 regions centred approximately on the equator and at right ascensions of 9^h, 12^h and $14^h.5$. These fields are known as G09, G12 and G15, respectively. Primary galaxy targets were selected from the DR6 (Adelman-McCarthy et al. 2008) of the SDSS (York et al. 2000) to extinction-corrected, Petrosian magnitude limits of $r < 19.4$ mag in the G09 and G15 fields and $r < 19.8$ mag in the G12 field.

We require Petrosian and model magnitudes and their errors in all five SDSS passbands in order to determine K-corrections (Section 2.5), and so we match objects in the GAMA team catalogue TilingCatv16 to objects in the SDSS DR6 PhotoObj table on SDSS ObjID using the SDSS CasJobs[1] service. We use only objects with GAMA survey_class ≥ 3 in order to exclude additional filler targets from the sample. We exclude objects, which, upon visual inspection, showed no evidence of galaxy light, were not the main part of a deblended galaxy, or had compromised photometry (vis_class = 2, 3 or 4, respectively). See Baldry et al. (2010) for further details of these target flags and Section 2.7 for a discussion of additional visual inspection of extreme-luminosity objects.

In estimating LFs, we use Petrosian magnitudes corrected for Galactic extinction according to the dust maps of Schlegel, Finkbeiner & Davis (1998). We make no attempt here to correct for intrinsic dust extinction within each galaxy, as was done by Driver et al. (2007), nor to extrapolate the Petrosian magnitudes to total, as done, for example, by Graham et al. (2005) and Hill et al. (2011). These systematic corrections to SDSS photometry, much more significant than any small random errors, will be considered in a subsequent paper.

An exception to our use of Petrosian magnitudes is for u-band data, where we instead use a pseudo-Petrosian magnitude defined by

$$u_{\text{pseudo-Petro}} = u_{\text{model}} - r_{\text{model}} + r_{\text{petro}}. \quad (1)$$

The reason for this is that the Petrosian u-band quantities are noisy and suffer from systematic sky-subtraction errors (Baldry et al. 2005). The pseudo-Petrosian u-band magnitude defined above, (using the SDSS r band since it has highest signal-to-noise ratio), and referred to as u_{select} by Baldry et al. (2005), is much better behaved at faint magnitudes.

For colour selection (see Section 2.6), we use SDSS model magnitudes in defining the $(g - r)$ colour, as recommended by the SDSS website.[2]

2.2 Spectroscopic observations

GAMA spectroscopic observations are described in the first GAMA data release paper (Driver et al. 2011). Observations for the GAMA Phase 1 campaign were made over 100 nights between 2008 February and 2010 May, comprising 493 overlapping $2°$ fields. Redshifts were assigned in a semi-automated fashion by the observers at the telescope. A subsequent re-redshifting exercise (Liske et al., in preparation) was used to assign a normalized quality nQ to each redshift, according to each particular observer and their assigned quality Q. Here we use reliable ($nQ > 2$) redshifts from all three

years of the GAMA Phase 1 campaign. In addition to pre-existing redshifts and those obtained with the Anglo-Australian Telescope, 20 redshifts of brighter galaxies were obtained with the Liverpool Telescope. The GAMA-II campaign, extending the survey to additional southern fields, began in 2011, but only GAMA-I redshifts are used here.

2.3 Completeness

Although GAMA has a very high spectroscopic completeness (>98 per cent; Driver et al. 2011), the small level of incompleteness is likely to preferentially affect low surface brightness, low-luminosity galaxies, or galaxies lacking distinctive spectral features. We have identified three sources of incompleteness that potentially affect the survey: the completeness of the input catalogue (imaging completeness), the completeness of the targets for which spectra have been obtained (target completeness) and the success rate of obtaining spectroscopic redshifts (spectroscopic success rate). These three sources of incompleteness, and how we correct for them, are now considered in turn.

2.3.1 Imaging completeness

Imaging completeness has been estimated for the SDSS main galaxy sample by Blanton et al. (2005b), who passed fake galaxy images through the SDSS photometric pipeline. Blanton et al. found that imaging completeness is nearly independent of apparent magnitude (at least down to $m_r \approx 18$ mag), depending mostly on r-band half-light surface brightness, $\mu_{50,r}$ (see their fig. 2). Thus, while GAMA goes about 2 mag fainter than the SDSS main galaxy sample, the Blanton et al. imaging completeness should still be approximately applicable. We have used their imaging completeness estimates modified in the following ways[3]:

(i) Blanton et al. determine imaging completeness over the surface brightness range $18 < \mu_{50,r} < 24.5$ mag arcsec^{-2}. Extrapolating their completeness as faint as $\mu_{50,r} = 26$ mag arcsec^{-2} results in negative completeness values. We therefore arbitrarily assume 1 per cent imaging completeness at $\mu_{50,r} = 26$ mag arcsec^{-2} and linearly interpolate from the faintest tabulated Blanton et al. completeness point at $(\mu_{50,r}, f_{\text{ph}}) = (24.34, 0.33)$.

(ii) The Blanton et al. imaging completeness decreases at the bright end, $\mu_{50,r} \lesssim 19$ mag arcsec^{-2}, due to a lower angular size limit of $\theta_{50} > 2$ arcsec and a star–galaxy separation criterion $\Delta_{\text{sg}} = r_{\text{psf}} - r_{\text{model}} > 0.24$ for the SDSS main galaxy sample which excludes some compact, high surface brightness (HSB) galaxies. GAMA target selection uses a far less stringent $\Delta_{\text{sg}} > 0.05$, backed up by $J - K$ colour selection, and so is much more complete in HSB galaxies. We therefore omit the Blanton et al. completeness points at $\mu_{50,r} < 19.2$ mag arcsec^{-2} and instead assume 100 per cent completeness at $\mu_{50,r} = 19.0$ mag arcsec^{-2} and brighter.

---

[1] http://casjobs.sdss.org/CasJobs/

[2] http://www.sdss.org/dr7/algorithms/photometry.html

[3] An alternative way of estimating imaging completeness is to determine what fraction of galaxies detected in the much deeper co-added data from SDSS Stripe 82 (Abazajian et al. 2009) are detected in regular, single-epoch SDSS imaging. However, one needs to allow for the large number of bright star or noise images misclassified as low surface brightness galaxies in the SDSS co-added catalogue, and so this approach was abandoned. It will be re-explored once high-quality VST-KIDS imaging of the GAMA regions becomes available.
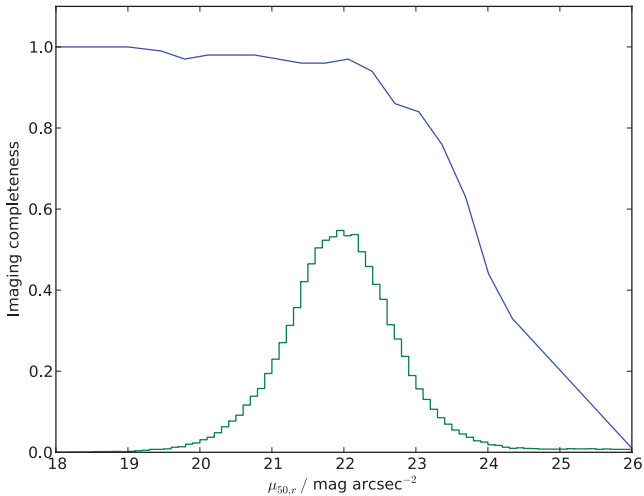
Figure 1. The top line shows imaging completeness as a function of *r*-band half-light surface brightness, $\mu_{50,r}$, from Blanton et al. (2005b), modified as described in the text. The histogram shows the normalized counts of $\mu_{50,r}$ for galaxies in the GAMA sample.

Our revised imaging completeness curve, along with a histogram of $\mu_{50,r}$ values for GAMA galaxies, is given in Fig. 1.

2.3.2 Target completeness

Target completeness in the *r* band may be assessed relative to the GAMA tiling catalogue, which contains all galaxies to $r = 19.8$ mag in the GAMA regions. In the *ugiz* bands, however, there is no well-defined magnitude limit. We therefore re-implement the GAMA target selection criteria detailed by Baldry et al. (2010) on samples

of objects selected from the SDSS DR6 PhotoObj table. We replace the Baldry et al. (2010) magnitude limits (their equation 6) with the following: $u < 21.0$, $g < 20.5$, $r < 20.0$, $i < 19.5$ or $z < 19.0$.

Target completeness in each band is then simply defined as the fraction of target galaxies that have been spectroscopically observed, either by GAMA or by another redshift survey, as a function of apparent magnitude in that band. This is shown in Fig. 2, where we have used magnitude bins which are equally spaced in $m' = 10^{0.52(m-m_{\min})}$. This binning is chosen to give a roughly equal number of galaxies per bin, thus avoiding large Poisson uncertainties at bright magnitudes. In the *r* band, target completeness is around 98–99 per cent brighter than $r = 19.4$ mag corresponding to the magnitude limit of the GAMA G09 and G15 fields.

In the other four bands, the drop in completeness at faint magnitudes is more gradual due to the spread in galaxy colours. Magnitude limits in each band are set to the faintest magnitude at which target completeness is at least 92 per cent (*u* band) or where completeness starts to drop rapidly. These magnitude limits are 20.3, 19.5, 19.4, 18.7, 18.2 in *ugiz*, respectively, and are indicated by the vertical dashed lines in Fig. 2.

An alternative approach to estimating the LF in bands other than that of target selection is to perform a multivariate LF (see e.g. Loveday 2000), or to use a $1/V_{\max}$ estimator where $V_{\max}$ is calculated using the selection-band magnitude (see e.g. Smith, Loveday & Cross 2009). While using more data, these estimators suffer from a colour bias as one approaches the sample flux limit, and so we prefer the more conservative approach adopted here.

2.3.3 Redshift success rate

The redshift success rate is most likely to depend on the flux that goes down a 2dF fibre, that is a seeing-convolved 2-arcsec-diameter aperture. The closest quantity available in the SDSS data base
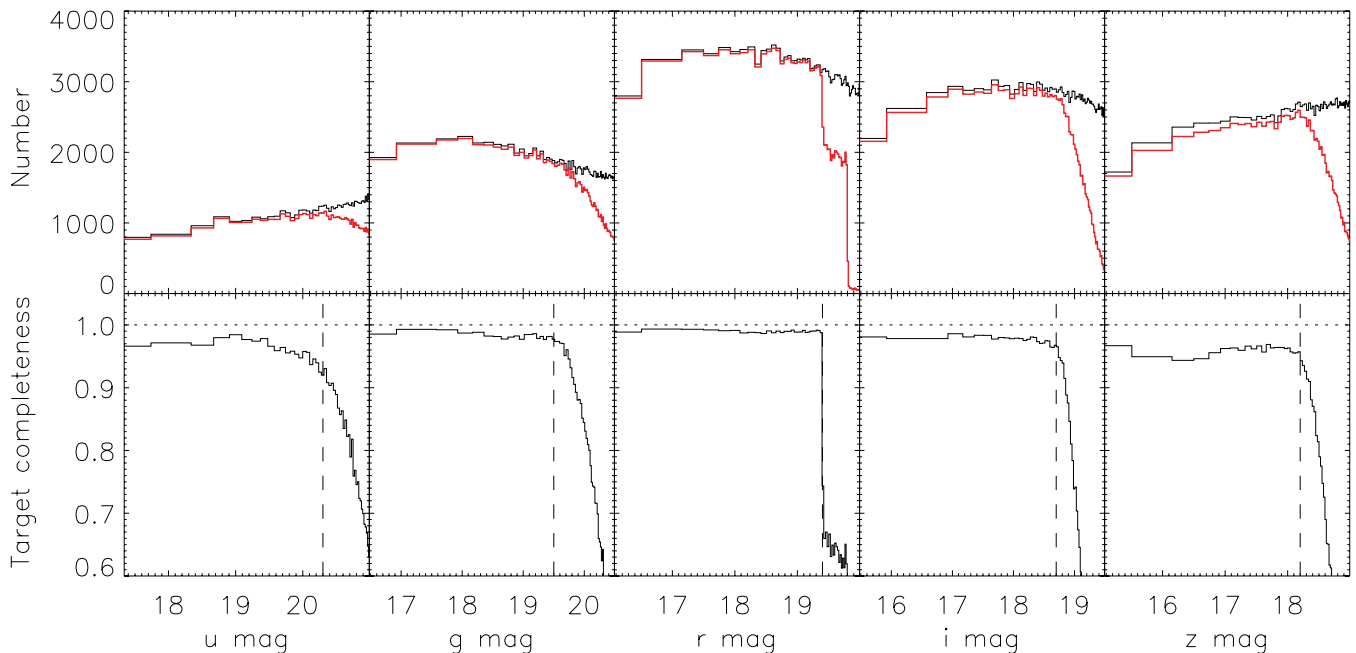

Figure 2. GAMA target completeness as a function of magnitude (pseudo-Petrosian for *u*, Petrosian for *griz*). The upper panels show galaxy counts in varying-width magnitude bins, chosen to give roughly equal numbers of galaxies per bin, for GAMA targets (thin black histogram) and counts for galaxies that have been spectroscopically observed (thick red histogram). The lower panels show target completeness, that is, the ratio of observed to target counts, with the horizontal dotted line indicating 100 per cent target completeness. The vertical dashed lines indicate our chosen magnitude limits in each band: 20.3, 19.5, 19.4, 18.7, 18.2 in *ugiz*, respectively.
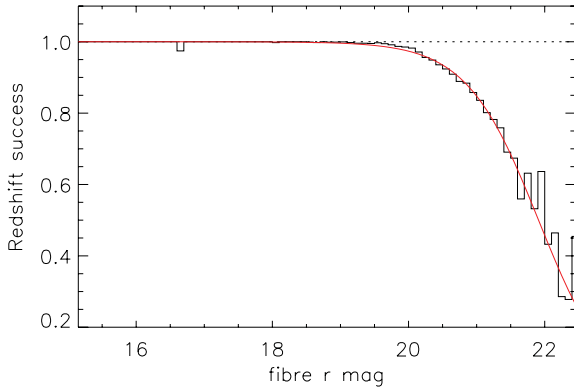
Figure 3. GAMA redshift success rate as a function of fibre *r*-band magnitude plotted as the black histogram, with the horizontal dotted line indicating 100 per cent success. The red curve shows the best-fitting sigmoid function.

is `fiberMag_r`, hereinafter r_{fibre}, corresponding to the flux contained within a 3-arcsec-diameter aperture centred on the galaxy. We therefore determine histograms of r_{fibre} (uncorrected for Galactic extinction) for all objects with high-quality redshifts ($nQ > 2$) and for all objects with spectra. The ratio of these two histograms then gives redshift success as a function of r_{fibre}, and is shown in Fig. 3. Note that some spectra observed in poor conditions have been re-observed at a later date in order to obtain this high success rate.

We see that the redshift success rate is essentially 100 per cent for $r_{fibre} < 19.5$, declines gently to around 98 per cent by $r_{fibre} = 20$ and then declines steeply at fainter magnitudes. We have fitted a sigmoid function $f = 1/[1 + e^{a(r_{fibre} - b)}]$ to the binned success rate. Sigmoid functions have previously been used to model survey completeness, for example, by Ellis & Bland-Hawthorn (2007). Our best-fitting sigmoid function has parameters $a = 1.89$ mag^{-1}, $b = 21.91$ mag, shown by the red line in Fig. 3, and we use this fit in determining the redshift success rate.

2.3.4 Galaxy weights

Each galaxy is given a weight which is equal to the reciprocal of the product of the imaging completeness, target completeness and redshift success rate. Imaging completeness C_{im} is determined from the galaxy's apparent *r*-band half-light surface brightness, $\mu_{50,r}$, by linear interpolation of the curve in Fig. 1. Target completeness C_{targ} is determined separately in each band from the galaxy's magnitude according to Fig. 2 and the spectroscopic success rate C_{spec} is determined from the sigmoid function fit described in Section 2.3.3.

The weight W_i assigned to galaxy *i* is then

$$W_i = 1/(C_{im} C_{targ} C_{spec}). \tag{2}$$

These weights, as a function of magnitude in each band, are shown for a randomly selected 5 per cent of galaxies in Fig. 4. The majority of galaxies brighter than our magnitude limits have weight $W_i < 1.1$, with a small fraction extending to $W_i \simeq 2$.

2.4 Velocity corrections

The redshifting software RUNZ (Saunders, Cannon & Sutherland 2004) provides heliocentric redshifts. Before converting heliocentric redshifts into any other velocity reference frame, we first eliminate likely stars from our sample by rejecting objects with a heliocentric redshift $z_{helio} < 0.002$ ($cz < 600$ km s^{-1}). This lower redshift cut is conservatively chosen, as the *2nd Catalogue of Radial Velocities with Astrometric Data* (Kharchenko et al. 2007) includes only one star with radial velocity RV > 500 km s^{-1}, and the vast majority of Galactic stars have RV < 200 km s^{-1}. Furthermore, fig. 7 of Driver et al. (2011) shows that the redshift-error distribution for GAMA is essentially zero by $cz = 600$ km s^{-1}.

Having eliminated 2111 likely stars from our sample, heliocentric redshifts are converted into the cosmic microwave background (CMB) rest frame z_{CMB} according to the dipole of Lineweaver et al. (1996). For nearby galaxies ($z_{CMB} < 0.03$), we apply the multiattractor flow model of Tonry et al. (2000). Note there are triple-valued solutions of $z_{CMB} \rightarrow z_{Tonry}$ over a small range in G12 (near the Virgo
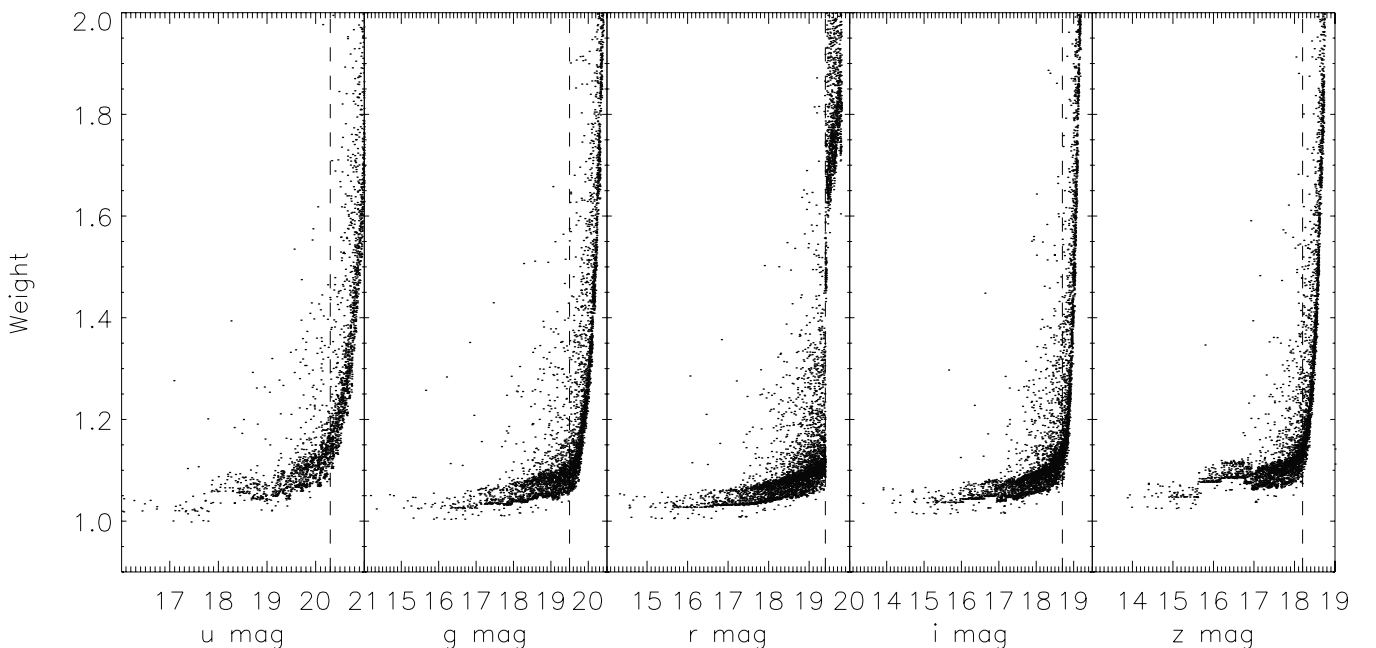

Figure 4. Completeness-correction weights as a function of magnitude for a random 5 per cent subset of GAMA galaxies. The vertical dashed lines show the magnitude limits applied in the LF analysis of each band.

cluster); here, the average distance is used. The solution is tapered to z_{CMB} from $z_{CMB} = 0.02$ to 0.03 (see Baldry et al. 2011 for details). We will see later that the Tonry et al. flow correction affects only the very faintest end of the LF.

2.5 K-corrections

When estimating intrinsic galaxy luminosities, it is necessary to correct for the fact that a fixed observed passband corresponds to a different range of wavelengths in the rest frames of galaxies at different redshifts, the so-called *K*-correction (Humason, Mayall & Sandage 1956). The *K*-correction depends on the passband used, the redshift of the galaxy and its SED. Here we use KCORRECT v4_2 (Blanton et al. 2003a; Blanton & Roweis 2007) in order to estimate and apply these corrections. Briefly, this code estimates an SED for each galaxy by finding the non-negative, linear combination of five template spectra that gives the best fit to the five SDSS model magnitudes of that galaxy. KCORRECT can then calculate the *K*-correction in any given passband at any redshift. Before calling KCORRECT itself, we use K_SDSSFIX to convert SDSS asinh magnitudes into the AB system and to add in quadrature to the random *ugriz* mag errors given in the SDSS data base typical systematic errors of (0.05, 0.02, 0.02, 0.02, 0.03) mag, respectively.

We determine *K*-corrections in a passband blueshifted by $z_0 = 0.1$. These magnitudes are indicated with a superscript prefix of 0.1, for example, $^{0.1}M_r$. This choice of rest frame allows direct comparison with most previously published LFs based on SDSS data.

Our LF estimators require *K*-corrections to be calculated for each galaxy at many different redshifts in order to work out visibility limits. To make this calculation more efficient, we fit a fourth-order polynomial $P_k(z) = \sum_{i=0}^{4} a_i(z - z_0)^i$, with $z_0 = 0.1$, to the $K(z)$ distribution for each galaxy and use this polynomial fit to determine *K*-corrections as a function of redshift. Using a polynomial of this order, the rms difference between the KCORRECT prediction and the polynomial fit is 0.01 mag or less in all five bands. Calculated *K*-corrections and their polynomial fits are shown for the first four galaxies in our sample, along with the median *K*-corrections and the 5 and 95 percentile ranges for the full sample, in Fig. 5.

Strictly, one should use heliocentric redshift when calculating *K*-corrections, since they depend on the *observed* passband. However, for consistency with finding the minimum and maximum redshifts at which a galaxy would still be visible when using the $1/V_{max}$ LF estimator, we use the flow-corrected redshift as described in Section 2.4. The difference in *K*-correction when using heliocentric or flow-corrected redshift is entirely negligible.

2.6 Colour subsamples

As well as analysing flux-limited samples of galaxies in the *ugriz* bands (hereinafter the combined sample), we separate the galaxies into blue and red subsamples. Following Zehavi et al. (2011), we use a colour cut based on the *K*-corrected $(g - r)$ model colour and absolute *r*-band magnitude that is insensitive to redshift:

$$^{0.1}(g - r)_{model} = 0.15 - 0.03^{0.1}M_r. \qquad (3)$$

We have adjusted the zero-point of 0.21 mag in Zehavi et al. (2011) to 0.15 mag in order to better follow the 'green valley' and to get more equal-sized samples of blue and red galaxies. This colour cut works well at all redshifts (Fig. 6), although we see that the colour bimodality becomes far less obvious beyond redshift $z = 0.2$ due to the lack of low-luminosity, blue galaxies at these high redshifts.
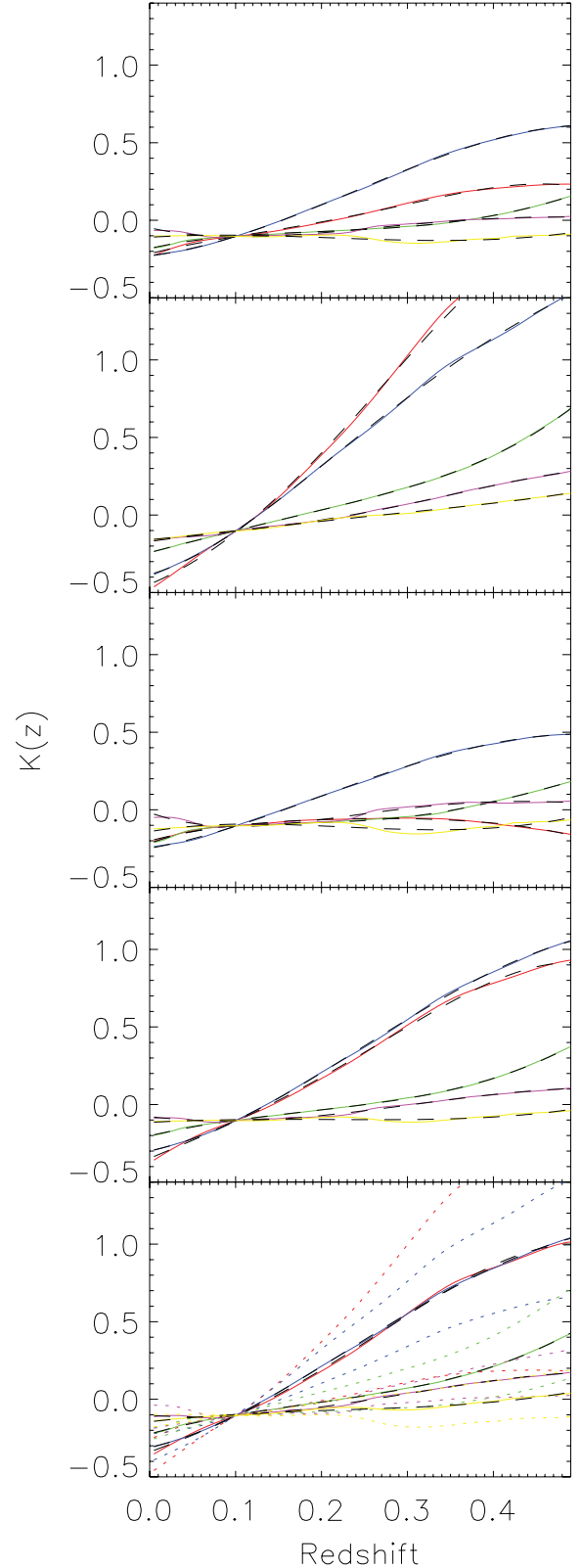

Figure 5. Top four panels: *K*-corrections as a function of redshift (red, blue, green, magenta and yellow, respectively, for *ugriz*) for the first four galaxies in our sample. The black dashed lines show fourth-order polynomial fits to each band. Bottom panel: median *K*-corrections (coloured continuous lines) and 5 and 95 percentile ranges (dotted lines) for the entire GAMA sample. The black dashed lines show fourth-order polynomial fits to the medians.
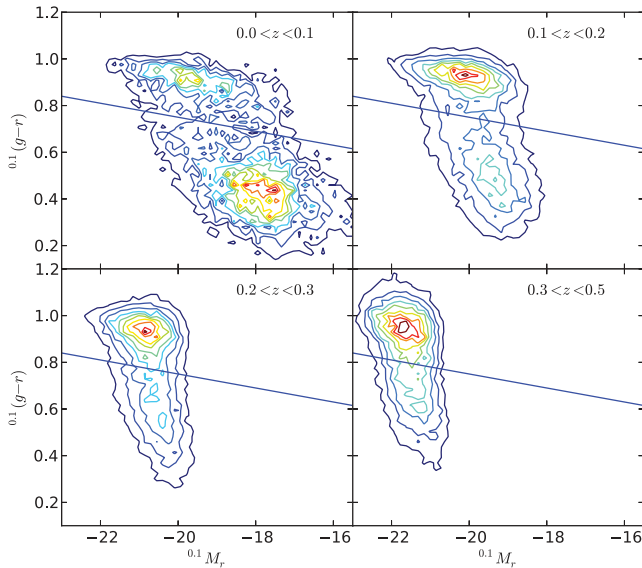
Figure 6. $^{0.1}(g-r)$ colour versus $^{0.1}M_r$ r-band absolute magnitude contour plots for GAMA galaxies in four redshift ranges as labelled. 10 contours, spaced linearly in density, are colour-coded from black to red in order of increasing density. The straight line shows the magnitude-dependent colour cut separating blue and red galaxies given by equation (3).

Table 1. Classification of extreme high- and low-luminosity objects.

post_class	$^{0.1}M_u < -20$ mag	$^{0.1}M_r > -15$ mag
1 OK	4743	299
2 QSO	18	0
3 Major shred	68	62
4 Minor shred	0	7
5 Problem deblend	151	16
6 Bad sky background	246	14

to the difficulty in distinguishing QSOs and compact blue galaxies from the imaging data alone.

(3) The central part of a galaxy which has been shredded into multiple detections. It is likely that the luminosity is somewhat underestimated in these cases.

(4) The target is a minor part of a shredded galaxy. Luminosity is likely to be greatly underestimated.

(5) The galaxy is very close to a second object which either has not been deblended or is likely to significantly affect the estimated luminosity in either direction.

(6) Photometry is likely severely compromised by rapidly varying sky background due typically to the presence of a nearby saturated star.

Examples of objects with these classifications are given in Fig. 7. In practice, there is some ambiguity in assigning a galaxy with classification 4 or 5, but as far as the LF analysis is concerned, it makes no difference.

These inspections were based on version 10 of the GAMA tiling catalogue, excluding objects with vis_class = 2–4. The major and minor shreds in Table 1 have also been inspected by IKB. In the case of major shreds, we have summed the flux from the components of the shredded galaxy to derive a 'deblend-fixed' magnitude. In total, 281 GAMA-I galaxies have had their magnitudes fixed in this manner.

In the case of six minor shreds, which both JL and IKB agreed on, the value of vis_class has been set equal to 3 in the latest version (v16) of the tiling catalogue.

The fractions of galaxies with post_class of 3 or 4 or higher as a function of M_u and M_r are shown in Fig. 8. We see in the left-hand panel that by magnitudes of $M_u = -20$, less than 10 per cent of objects have suspect photometry. Once we allow for fixing of overdeblended galaxies, a similar fraction of objects with $M_r \simeq -15$ have suspect photometry (right-hand panel).

For our analysis, we have chosen to exclude any galaxies with post_class of 4 or higher, that is, we include major shreds with fixed fluxes but exclude minor shreds, problem deblends and bad sky objects. Fig. 9 shows the ratio of the r- and u-band LFs using post_class < 4 galaxies to that determined using all galaxies. We see that excluding objects with suspect photometry has a relatively minor effect on the determined LF: the very bright end and some faint-end bins are systematically lower by up to 50 per cent; these changes are comparable to the size of the error bars.

Finally, we note that Brough et al. (2011) have independently checked a sample of GAMA galaxies with the lowest detected Hα luminosity. Our four faintest r-band luminosity galaxies are also in the Brough et al. sample.

Although colour bimodality is more pronounced in the $(u-r)$ colour (see e.g. Strateva et al. 2001; Baldry et al. 2004), u-band photometry, even after forming a 'pseudo-Petrosian' magnitude (equation 1) is rather noisy, and so we prefer to base our colour cuts on the more robust $(g-r)$ colour. This colour cut (in the original form of Zehavi et al.) has also been used to investigate the angular clustering of galaxies by Christodoulou et al. (2011). One should also note that colour is not a proxy for galaxy morphology: many red galaxies are in fact dust-obscured disc galaxies (Driver et al., in preparation).

2.7 Outlier inspection

We measure the LF over a very wide range of luminosities, -23 to -11 mag, in the r band. Galaxies at the extremes of this luminosity range are very rare in a flux-limited survey, due either to their intrinsic low number density at high luminosity or to small detection volume at low luminosity, and thus it is likely that a significant fraction of these putative extreme objects are in fact artefacts due to incorrectly assigned redshifts or magnitudes. The first author has therefore inspected image cut-outs showing SDSS image detections of 5226 very luminous GAMA targets with $^{0.1}M_u < -20$ mag and 398 very faint targets with $^{0.0}M_r > -15$ mag. We choose the u band to select luminous outliers since the u-band LF shows the largest bright-end excess.

Table 1 shows how the inspected images were classified. The classification codes, which we call post_class in order to distinguish them from the pre-target-selection vis_class, have the following meanings:

(1) OK – nothing from the image would lead one to expect poor photometry for that object.

(2) The object looks like a quasar (QSO), that is, blue and point like. This classification is ignored in the analysis (treated as OK) due
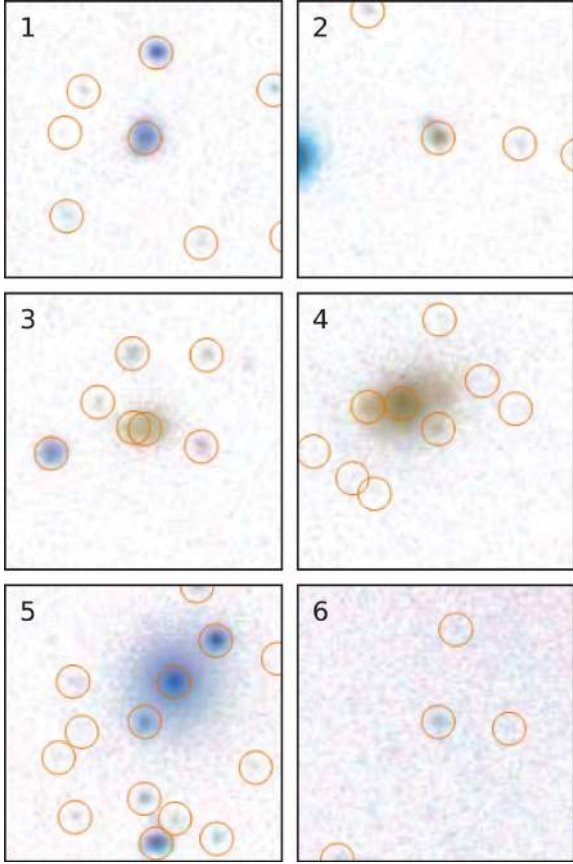
Figure 7. Examples of objects classified from 1 to 6. The GAMA targets are at the centre of each image, which are 40 arcsec on each side. The colour table has been inverted, so that red objects appear blue and vice versa, in order to obtain a light background. The circles denote SDSS image detections: multiple circles on a single object [example classifications 3 and 4] suggest that it has been overdeblended. post_class classifications are shown in the top left-hand corner of each image; their meaning is given in Table 1.
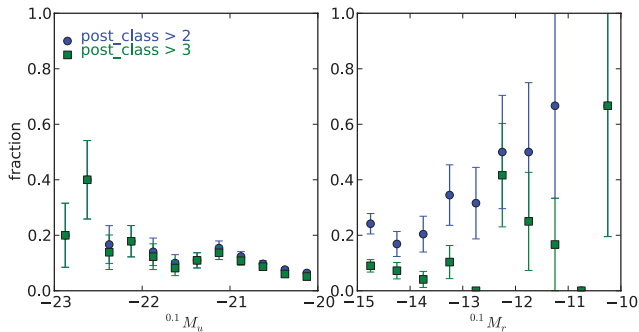

Figure 8. Fraction of objects with post_class > 2 (blue circles) and >3 (green squares) as a function of $^{0.1}M_u$ (left-hand panel) and $^{0.1}M_r$ (right-hand panel). The error bars show Poisson errors on the counts.

3 ESTIMATING THE LUMINOSITY FUNCTION AND ITS EVOLUTION

3.1 Parametrizing the evolution

In order to parametrize the evolution of the galaxy LF, we follow Lin et al. (1999) in assuming a Schechter (1976) function in which the characteristic magnitude M^* and galaxy density ϕ^* are allowed
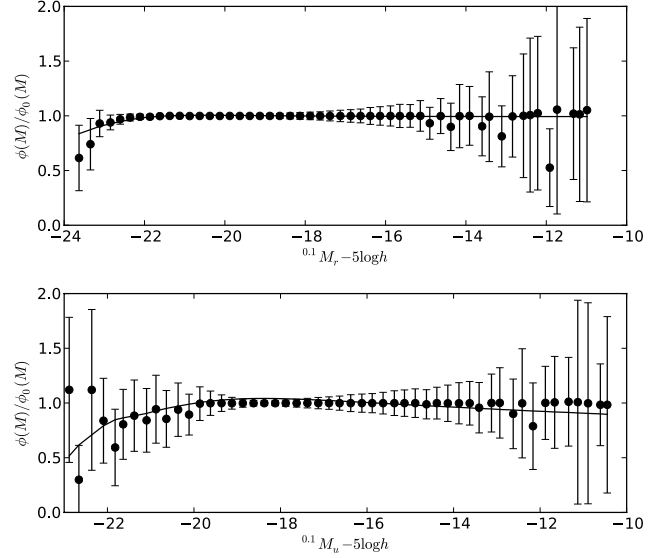

Figure 9. Ratio of LFs determined using post_class ≤ 3 objects to that using all objects in the r band (top panel) and u band (bottom panel). The symbols show the ratio of SWML estimates and their uncertainties and the continuous lines show the ratio of parametric fits to the two samples.

to vary with redshift, but where the faint-end slope α is assumed to be non-evolving.[4]

Specifically, in magnitudes, the Schechter function is given by

$$\phi(M) = 0.4 \ln 10 \phi^* (10^{0.4(M^*-M)})^{1+\alpha} \exp(-10^{0.4(M^*-M)}), \quad (4)$$

where the Schechter parameters α, M^* and ϕ^* vary with redshift as

$$\alpha(z) = \alpha(z_0),$$
$$M^*(z) = M^*(z_0) - Q(z - z_0),$$
$$\phi^*(z) = \phi^*(0)10^{0.4Pz}. \quad (5)$$

Here the fiducial redshift z_0 is the same redshift to which magnitudes are K-corrected, in our case $z_0 = 0.1$. The Schechter parameters α, $M^*(z_0)$ and $\phi^*(0)$, and evolution parameters Q and P are determined via the maximum-likelihood methods described by Lin et al. (1999).

First, the shape parameters α and $M^*(z_0)$, and luminosity evolution parameter Q are fitted simultaneously and independently of the other parameters by maximizing the log-likelihood

$$\ln \mathcal{L} = \sum_{i=1}^{N_{\text{gal}}} W_i \ln p_i. \quad (6)$$

Here, W_i is the incompleteness correction weighting (equation 2) and the probability of galaxy i having absolute magnitude M_i, given its redshift z_i, is

$$p_i \equiv p(M_i|z_i) = \phi(M_i) \bigg/ \int_{\max[M_{\min}(z_i),M_1]}^{\min[M_{\max}(z_i),M_2]} \phi(M)\,\mathrm{d}M, \quad (7)$$

where M_1 and M_2 are the absolute magnitude limits of the sample, $M_{\min}(z_i)$ and $M_{\max}(z_i)$ are the minimum and maximum absolute

---

[4] Evolution in the LF faint-end slope α with redshift is still rather poorly constrained. Ellis et al. (1996) claim that α steepens with redshift, due to an increase in the number of faint, star-forming galaxies at $z \simeq 0.5$. Ilbert et al. (2005) also measure a possible steepening of α with redshift. In contrast, Liu et al. (2008) find that α gets shallower at higher redshifts. Our assumption of fixed α is largely based on practical necessity, since α can only be reliably measured at redshifts $z \lesssim 0.2$ from the GAMA data.

magnitudes visible at redshift z_i, and $\phi(M)$ is the differential LF given by equation (4).

The density evolution parameter P and normalization $\phi^*(0)$ cancel in the ratio in equation (7) and so must be determined separately. Lin et al. show that the parameter P may be determined by maximizing the second likelihood

$$\ln \mathcal{L}' = \sum_{i=1}^{N_{gal}} W_i \ln p_i',$$ (8)

where

$$p_i' \equiv p[z_i | M_i(0), Q]$$
$$= 10^{0.4Pz_i} \bigg/ \int_{\max[z_{\min}[M_i(0)], z_1]}^{\min[z_{\max}[M_i(0), z_2]]} 10^{0.4Pz} \frac{dV}{dz} dz ,$$ (9)

where z_1 and z_2 are the redshift limits of the sample, and $z_{\min}$ and $z_{\max}$ are the redshift limits over which galaxy i may be observed, given the survey's apparent magnitude limits and its absolute magnitude evolution-corrected to redshift zero, $M_i(0) = M_i(z_i) + Qz_i$. Note that the value of P is independent of the fiducial redshift z_0.

Finally, we fit for the overall normalization $\phi^*(0)$. We depart slightly from the prescription of Lin et al. (1999) here. In place of their equation (14), we use a minimum variance estimate of the space density $\bar{n}$ of galaxies:

$$\bar{n} = \sum_{i=1}^{N_{gal}} \frac{W_i U(z_i)}{10^{0.4Pz_i}} \bigg/ \int_{z_{\min}}^{z_{\max}} \frac{dV}{dz} S(z) U(z) \, dz ,$$ (10)

where $S(z)$ is the galaxy selection function, $U(z)$ is a redshift weighting function chosen to give minimum variance and dV/dz is the volume element at redshift z. The selection function for galaxies with luminosities L_1 to L_2 is

$$S(z) = \int_{\max(L_{\min}(z), L_1)}^{\min(L_{\max}(z), L_2)} \phi(L, z) dL \bigg/ \int_{L_1}^{L_2} \phi(L, z) \, dL .$$ (11)

Note that the integration limits in the numerator depend on the assumed K-correction. In this case, we use the median K-correction of the galaxies in the sample under consideration: see Fig. 5 for median K-corrections for the full sample as a function of redshift. Our results change by much less than the estimated 1σ errors (see Section 3.5) if we use mean instead of median K-corrections.

We adopt the redshift weighting function

$$U(z) = \frac{1}{1 + 4\pi(\bar{n}/\bar{W})J_3(r_c)S(z)}, \quad J_3(r_c) = \int_0^{r_c} r^2 \xi(r) \, dr, \quad (12)$$

where $\xi(r)$ is the two-point galaxy correlation function and $\bar{W}$ is the mean incompleteness weighting. Provided $J_3(r_c)$ converges on a scale r_c much smaller than the depth of the survey, this redshift weighting scheme (equation 12) minimizes the variance in the estimate of $\bar{n}$ (Davis & Huchra 1982). Larger values of J_3 weight galaxies at high redshift more highly; we assume $4\pi J_3 = 30\,000\,h^{-3}\,\mathrm{Mpc}^3$. This value comes from integrating the flux-limited two-point galaxy correlation function of Zehavi et al. (2005), $\xi(r) = (r/5.59)^{-1.84}$, to $r_c = 60\,h^{-1}$ Mpc; at larger separations the value of J_3 becomes uncertain. However, the results are not too sensitive to the value of J_3, the estimated densities changing by less than 8 per cent if J_3 is halved. This possible systematic error is generally comparable to or less than the statistical uncertainty in ϕ^* (5–25 per cent).

We check our minimum variance normalization by comparing, in Tables 3–5 given below, the observed number of galaxies in each sample (within the specified apparent magnitude, absolute

magnitude and redshift limits) with the prediction

$$N_{pred} = \frac{1}{\bar{W}} \int_{z_{\min}}^{z_{\max}} \int_{L_{\min}(z)}^{L_{\max}(z)} \phi(L, z) \frac{dV}{dz} dz.$$ (13)

3.2 Luminosity density

Given our assumed evolutionary model, the predicted LD is given by

$$\rho_{L\,fit} = \rho_L(0)10^{0.4(P+Q)z},$$ (14)

(Lin et al. 1999, equation 11), where

$$\rho_L(0) = \int L\phi(L, z = 0)dL = \phi^*(0)L^*(0)\Gamma(\alpha + 2),$$ (15)

and $\Gamma(x)$ is the standard Gamma function. In making this prediction, we are integrating over all possible luminosities, and hence extrapolating our Schechter function fits. This extrapolation introduces no more than 1 per cent in additional LD beyond that contained within our luminosity limits. We obtain luminosities in solar units using the following absolute magnitudes for the Sun in the SDSS bandpasses: $^{0.1}M_{\odot u,g,r,i,z} - 5\log h = 6.80, 5.45, 4.76, 4.58, 4.51$ mag (Blanton et al. 2003b), respectively.

We also directly determine LD as a function of redshift by summing the weighted luminosities of galaxies in a series of redshift bins:

$$\rho_{L\,j} = \frac{1}{V_j} \sum_{i \in j} \frac{W_i L_i}{S_L(z_i)}.$$ (16)

(Lin et al. 1999, equation 16). Here V_j is the volume of redshift bin j, the sum is over each galaxy i in bin j and the factor

$$S_L(z) = \int_{\max(L_{\min}(z), L_1)}^{\min(L_{\max}(z), L_2)} L\phi(L, z)dL \bigg/ \int_0^{\infty} L\phi(L, z)dL ,$$ (17)

(Lin et al. 1999, equation 17) extrapolates for the luminosity of galaxies lying outside the accessible survey flux limits.

3.3 Binned LF estimates

In order to assess how well the model (equation 5) parametrizes LF evolution, we also make non-parametric, binned, estimates of the LF in independent redshift ranges using the $1/V_{\max}$ (Schmidt 1968; Eales 1993) and stepwise maximum likelihood (SWML, Efstathiou, Ellis & Peterson 1988) methods. We use 60 magnitude bins from $M = -25$ to -10 with $\Delta M = 0.25$ and a series of redshift slices.

When estimating the LF over restricted redshift ranges, one has to be careful to only include magnitude bins that are fully sampled, since otherwise the LF will be underestimated in incompletely sampled bins (see Fig. 10). We therefore set the following magnitude limits for each redshift slice so that only complete bins are included:

$$M_{faint} < m_{faint} - DM(z_{lo}) - K(z_{lo}),$$
$$M_{bright} > m_{bright} - DM(z_{hi}) - K(z_{hi}).$$ (18)

Here, m_{faint} and m_{bright} are the flux limits of the survey, $DM(z)$ is the distance modulus, $K(z)$ is the K-correction for a galaxy with the median SED of those in the survey, z_{lo} and z_{hi} are the limits of the redshift slice under consideration, and M_{faint} and M_{bright} are the absolute magnitude limits of each bin. A bin should only be included if it satisfies both equations (18).

Again following Lin et al. (1999), we incorporate the galaxy incompleteness weights into the SWML maximum likelihood estimator by multiplying each galaxy's log-probability by its weight
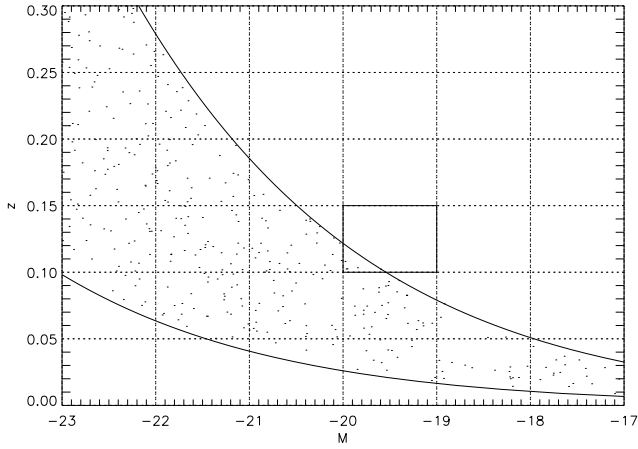
Figure 10. Illustration of estimating $\phi(M, z)$ in bins of absolute magnitude M and redshift z represented by the dotted lines for a fictitious survey with apparent magnitude limits $m_{bright} = 14.5$ and $m_{faint} = 18$. Galaxies (represented by the points) are of course only found between these flux limits, corresponding to the lower and upper curved lines, respectively. Now consider the highlighted bin, centred on $M = -19.5$ and with redshift limits $z_{lo} = 0.10$, $z_{hi} = 0.15$. At the lower redshift limit, the absolute magnitude corresponding to m_{faint} is $M \simeq -19.6$. Since this is the mid-bin, the LF estimated for this bin would be underestimated, and therefore the bin should be excluded. Thus, for the redshift slice $0.10 < z < 0.15$, only magnitude bins brightwards of $M = -20$ should be used. (The fact that the magnitude bin centred on $M = -20.5$ is incomplete at redshifts $z > z_{lo}$ will be compensated for by $1/V_{max}$ weighting.) A similar incompleteness may arise for bins at low redshift and high luminosity. For the redshift slice $0.00 < z < 0.05$, only magnitude bins *fainter* than $M = -21$ should be used.

before summing to form a log-likelihood (equation 6). In the $1/V_{max}$ estimate, we form a sum of the weight of each galaxy divided by the volume within which it is observable. We normalize the SWML estimates ϕ_{SWML} in each redshift slice to the $1/V_{max}$ estimates $\phi_{V_{max}}$ by imposing the constraint

$$\sum_{k=1}^{N_{bin}} \phi_{SWML_k} V(M_k) = \sum_{k=1}^{N_{bin}} \phi_{V_{max}k} V(M_k), \tag{19}$$

where $V(M_k)$ is the volume (within the redshift limits of each slice) over which a galaxy of absolute magnitude M_k, being the mean galaxy absolute magnitude in bin k, is visible. The predicted number of galaxies

$$N_{SWML} = \frac{1}{\overline{W}} \sum_{k=1}^{N_{bin}} \phi_k V(M_k) \Delta M \tag{20}$$

may also be compared with the observed number of galaxies within each redshift range.

We can use our SWML LF estimates to assess the quality of the parametric fits using a likelihood ratio test (Efstathiou et al. 1988). In this test, we compare the log-likelihoods $\ln \mathcal{L}_1$ and $\ln \mathcal{L}_2$ given by equation (6) for the SWML and parametric estimates, respectively. The log-likelihood ratio $-2\ln(\mathcal{L}_1/\mathcal{L}_2)$ is expected to follow a χ^2 distribution with $\nu = N_p - 4$ degrees of freedom. Here N_p is the number of bins in the stepwise estimate and we subtract 1 degree of freedom for each of the fitted shape parameters α, $M^*(0)$ and Q and for the arbitrary normalization.

To allow for the finite bin sizes and redshift ranges of the SWML estimates, we calculate binned estimates of the parametric fits.

These are given by (Lin et al. 1999)

$$\phi_k^{z_1-z_2} = \frac{\int_{M_k-\Delta M/2}^{M_k+\Delta M/2} \int_{\max[z_{min}(M),z_1]}^{\min[z_{max}(M),z_2]} \phi^2(M, z) \frac{dV}{dz} dz \, dM}{\int_{M_k-\Delta M/2}^{M_k+\Delta M/2} \int_{\max[z_{min}(M),z_1]}^{\min[z_{max}(M),z_2]} \phi(M, z) \frac{dV}{dz} dz \, dM}. \tag{21}$$

Here, the parametric LF $\phi(M, z)$ is weighted by the number of galaxies at each magnitude and redshift, given by the factor $\phi(M, z)\frac{dV}{dz}$. These binned versions of the parametric fits are also used when plotting the LFs. For absolute magnitudes in all plots, we use the weighted mean magnitude of the galaxies in each bin, rather than using the magnitude of the bin centre. This helps to overcome the bias due to the finite width of magnitude bins.

3.4 LF faint end

It is now widely recognized that a Schechter function provides a poor fit to galaxy LFs when measured over a wide range of magnitudes (e.g. Blanton et al. 2005b). In order to parametrize the faint end, we separately analyse a low-redshift ($z < 0.1$) subset of the data and fit (non-evolving) double-power-law Schechter functions.

We use the parametrization of Loveday (1997), namely

$$\phi(L) = \phi^* \left(\frac{L}{L^*}\right)^\alpha \exp\left(\frac{-L}{L^*}\right) \left[1 + \left(\frac{L}{L_t}\right)^\beta\right]. \tag{22}$$

In this formulation, the standard Schechter function is multiplied by the factor $[1 + (L/L_t)^\beta]$, where $L_t < L^*$ is a transition luminosity between two power laws of slope α ($L \ll L_t$) and $\alpha + \beta$ ($L \gg L_t$). It is fitted to unbinned data using an extension to the method of Sandage, Tammann & Yahil (1979). With this four-parameter fit (the normalization ϕ^* is fitted separately), one has to be careful to choose sensible starting values in order for the downhill simplex algorithm (`scipy.optimize.fmin`) not to get stuck in local minima of $-\ln \mathcal{L}$. (We also found that it helped to call the minimizer several times, using 'best-fitting' parameters from one function call as starting parameters for the next; $-\ln \mathcal{L}$ was found to converge with two to four calls of the minimizer.)

Note that the double-power-law Schechter function may equivalently be written as the sum of two Schechter functions, for example, Blanton et al. (2005b) and Baldry, Glazebrook & Driver (2008), a fact which comes in useful when integrating the LF.

When fitting a double-power-law Schechter function, the likelihood ratio test has $\nu = N_p - 5$ degrees of freedom (cf. Section 3.3).

3.5 Error estimates

Schechter and evolution parameter estimates are strongly correlated, and so in Section 4 we present 95 per cent likelihood contour plots of the shape parameters α, M^*, β and M_t, and evolution parameters Q and P. For uncertainties in tabulated measurements, we estimate errors using the jackknife technique, as follows. We divide the GAMA survey area into nine regions, each $4 \times 4 \deg^2$. We then calculate the LF and LD using the methods discussed above, omitting each region in turn. For any parameter x, we may then determine its variance using

$$\text{Var}(x) = \frac{N-1}{N} \sum_{i=1}^{N} (x_i - \bar{x})^2, \tag{23}$$

where $N = 9$ is the number of jackknife regions and $\bar{x}$ is the mean of the parameters x_i measured while excluding region i. The jackknife method has the advantage of providing error estimates which include both uncertainties in the fitted parameters and sample variance.

The sample variance in galaxy density n may also be determined using

$$\left(\frac{\delta n}{n}\right)^2 = \frac{4\pi J_3}{V}, \tag{24}$$

(Davis & Huchra 1982; Efstathiou et al. 1988), where J_3 is defined in equation (12) and V is the volume of each sample between redshift limits.

For errors on binned LFs, we use Poisson errors for $1/V_{max}$ estimates and an inversion of the information matrix for SWML estimates (Efstathiou et al. 1988).

4 RESULTS

Before presenting our main results, we first check the effects of correcting for imaging completeness and the choice of flow model in converting redshifts into distances.

4.1 Imaging completeness correction

In Fig. 11, we compare r-band LFs calculated for the combined sample, with distances calculated using the Tonry et al. (2000) multiattractor flow model, with and without the correction for imaging completeness described in Section 2.3.1. As expected, we see that applying imaging completeness corrections boosts the LF faint end, while barely changing the bright end. The changes in fitted Schechter parameters due to imaging completeness corrections are tabulat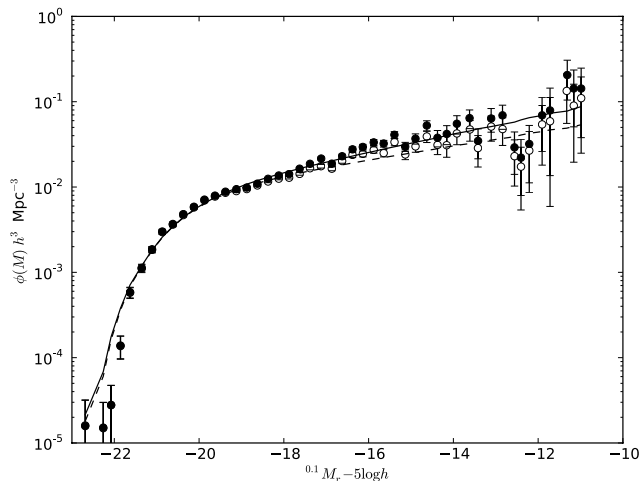ed in Table 2. Future plots and tabulated parameters will include imaging completeness corrections; approximate uncorrected Schechter parameters may be obtained by subtracting the appropriate quantities listed in Table 2.

Figure 11. LF estimates in the r band for low-redshift galaxies ($z < 0.1$) with (solid symbols and solid line) and without (open symbols and dashed line) applying a correction for imaging completeness. The symbols show SWML estimates and the lines show best-fitting Schechter functions.

Table 2. Change in fitted Schechter parameters for combined samples when applying imaging completeness correction.

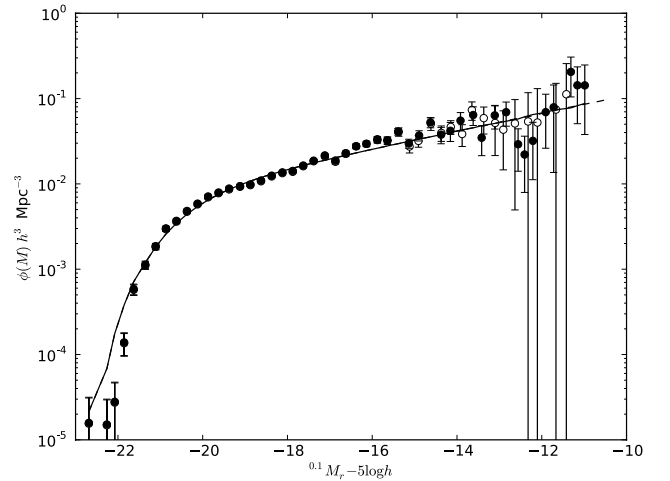| Band	$\Delta\alpha$	ΔM^*/mag	$\Delta\phi^*/h^3\,\mathrm{Mpc}^{-3}$
u	-0.05	-0.03	$0.000\,17$
g	-0.05	-0.04	$-0.000\,31$
r	-0.06	-0.07	$-0.000\,62$
i	-0.05	-0.06	$-0.000\,51$
z	-0.03	-0.03	$-0.000\,11$

Figure 12. LF estimates in the r band for low-redshift galaxies ($z < 0.1$) using the CMB reference frame (open circles) and the Tonry et al. (2000) multiattractor flow model (filled circles) using the SWML estimator. The solid and dashed lines show the best-fitting Schechter functions which are indistinguishable.

clude imaging completeness corrections; approximate uncorrected Schechter parameters may be obtained by subtracting the appropriate quantities listed in Table 2.

4.2 Effects of velocity flow model

Luminosities of galaxies at the extreme faint end of the LF, being very close by, will be sensitive to peculiar velocities. In Fig. 12, we compare r-band LFs calculated using the CMB reference frame (Lineweaver et al. 1996) and the Tonry et al. (2000) multiattractor flow model for galaxies at low redshift ($z < 0.1$). We see that the CMB-frame and flow model LFs only begin to differ at the extreme faint end, $M_r - 5\log h \gtrsim -15$ mag, and even at these faint magnitudes the differences are not large, given the size of the error bars. In particular, the recovered Schechter parameters are indistinguishable between the two velocity frames. Subsequent analysis will use the Tonry et al. flow model to determine luminosities.

4.3 Luminosity function faint end

Having looked at the effects of incompleteness and flow corrections, we now study in detail the faint end of the LF for low-redshift ($z < 0.1$) galaxies. Fig. 13 shows the LFs for our three (combined, blue and red) samples in the *ugriz* bands. Also shown are LFs corrected for surface brightness incompleteness by Blanton et al. (2005b) from the New York University Value-Added Galaxy Catalog low-redshift sample (Blanton et al. 2005a). Since these Blanton et al. LFs were calculated using rest-frame K-corrections, we apply an offset of $2.5\log(1 + z_0)$ to their absolute magnitudes in order to convert into our $z_0 = 0.1$ band-shifted K-corrections. Our faint-end LFs are systematically lower than those of Blanton et al., particularly in the u band. The difference can largely be explained by the different flow models used by Blanton et al. and in the present analysis. Reanalysing the Blanton et al. data using the Tonry et al. flow model results in much better agreement (Baldry et al. 2011) – the extra 1.7 mag depth of the GAMA versus SDSS main galaxy sample means that uncertainties due to the flow model affect the measured LF only at a correspondingly fainter magnitude.
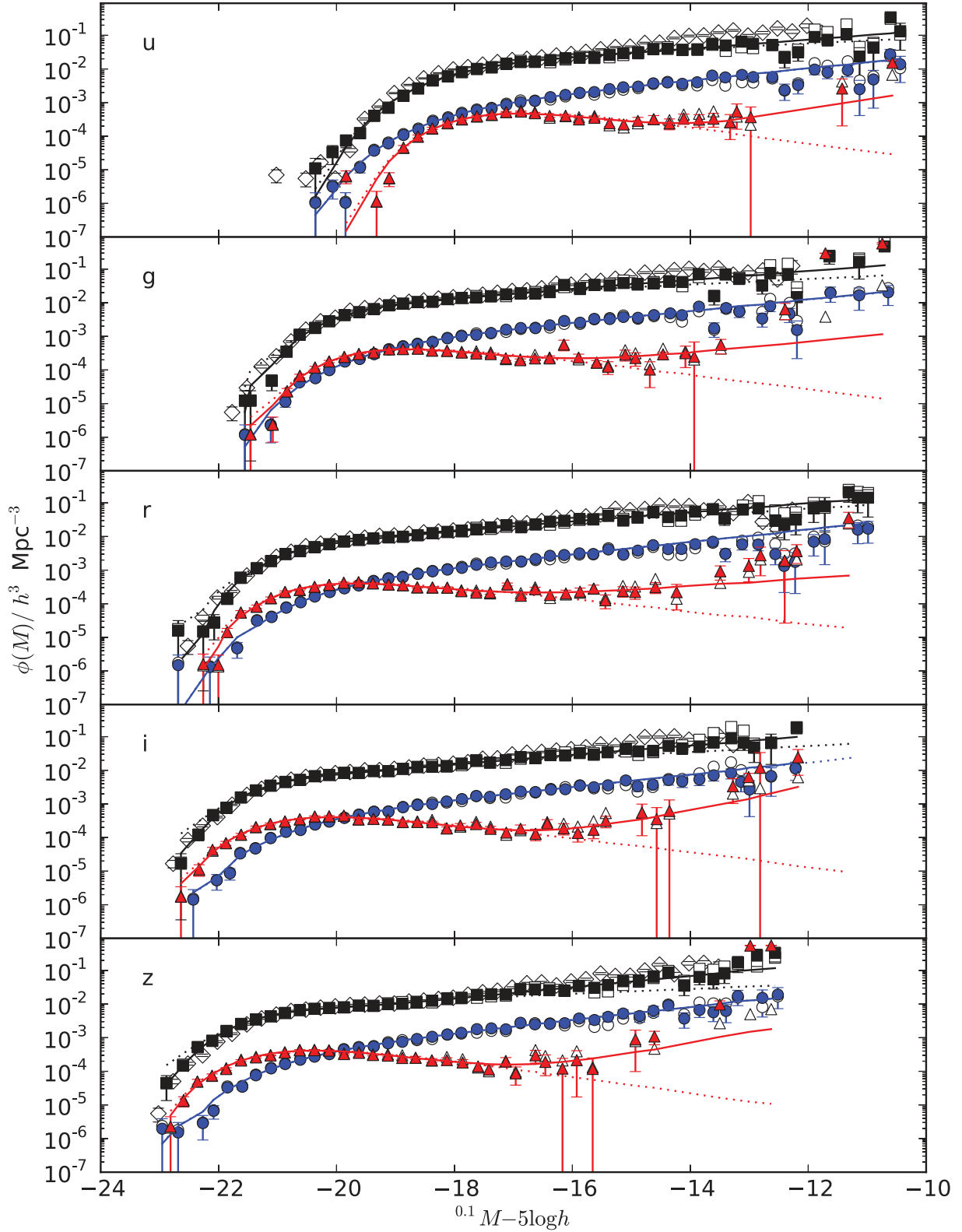
Figure 13. *ugriz* LFs at low redshift ($z < 0.1$). The black squares show SWML estimates for combined red and blue samples, and the blue circles and red triangles show SWML LFs for the blue and red samples, respectively. The open symbols of the same shapes show the corresponding $1/V_{max}$ estimates – these are hidden beneath the SWML estimates for all but the very faintest galaxies. The continuous lines show the best-fitting non-evolving double-power-law Schechter function fits and the dotted lines show standard Schechter function fits. LFs for the blue and red samples have been scaled by a factor of 0.1 to aid legibility. The open diamonds show the 'corrected' LF (without colour selection) from Blanton et al. (2005b).

Table 3. Standard Schechter function fits for low-redshift galaxies. Samples are as given in the first column. $^{0.1}M_1$ and $^{0.1}M_2$ are the absolute magnitude limits, N_{gal} is the number of galaxies in the sample and N_{pred} is the predicted number of galaxies from integrating the LF (equation 13). α, $^{0.1}M^*$ and ϕ^* are the usual Schechter parameters, and P_{fit} gives the probability of the Schechter function describing the observed LF determined from the likelihood ratio test described in the text. The luminosity densities ρ_{Lfit} and ρ_{Lsum} are calculated from equations (15) and (16), respectively.

	$^{0.1}M_1$ $-5\log h$	$^{0.1}M_2$	N_{gal}	N_{pred}	α	$^{0.1}M^* - 5\log h$	$\phi^* \times 100$ /h^3 Mpc^{-3}	P_{fit}	ρ_{Lfit}	ρ_{Lsum} /10^8 L$_\odot$ h Mpc^{-3}
All										
u	-21.0	-10.0	9181	9402 ± 766	-1.21 ± 0.03	-18.02 ± 0.04	1.96 ± 0.15	0.001	1.95 ± 0.18	1.95 ± 0.18
g	-22.0	-10.0	11158	$11\,085 \pm 781$	-1.20 ± 0.01	-19.71 ± 0.02	1.33 ± 0.12	0.000	1.79 ± 0.14	1.79 ± 0.15
r	-23.0	-10.0	12860	$12\,789 \pm 956$	-1.26 ± 0.02	-20.73 ± 0.03	0.90 ± 0.07	0.000	1.75 ± 0.15	1.75 ± 0.15
i	-23.0	-11.0	10438	$10\,341 \pm 745$	-1.22 ± 0.01	-21.13 ± 0.02	0.90 ± 0.08	0.000	2.06 ± 0.18	2.06 ± 0.18
z	-24.0	-12.0	8647	8535 ± 658	-1.18 ± 0.03	-21.41 ± 0.05	0.90 ± 0.06	0.000	2.39 ± 0.22	2.38 ± 0.22
Blue										
u	-21.0	-10.0	6278	6664 ± 509	-1.44 ± 0.02	-18.27 ± 0.04	0.88 ± 0.05	0.028	1.50 ± 0.14	1.52 ± 0.14
g	-22.0	-10.0	7356	7611 ± 537	-1.42 ± 0.02	-19.58 ± 0.05	0.71 ± 0.03	0.002	1.12 ± 0.10	1.12 ± 0.10
r	-23.0	-10.0	8579	8893 ± 680	-1.45 ± 0.02	-20.28 ± 0.07	0.55 ± 0.03	0.000	0.92 ± 0.09	0.92 ± 0.09
i	-23.0	-11.0	6432	6641 ± 465	-1.45 ± 0.02	-20.68 ± 0.06	0.50 ± 0.03	0.381	1.02 ± 0.09	1.02 ± 0.09
z	-24.0	-12.0	4888	5089 ± 400	-1.48 ± 0.03	-20.99 ± 0.07	0.41 ± 0.02	0.477	1.11 ± 0.11	1.10 ± 0.11
Red										
u	-21.0	-10.0	2903	2850 ± 263	-0.40 ± 0.08	-17.34 ± 0.06	1.29 ± 0.12	0.000	0.52 ± 0.05	0.53 ± 0.05
g	-22.0	-10.0	3802	3758 ± 307	-0.47 ± 0.07	-19.31 ± 0.06	1.06 ± 0.11	0.000	0.75 ± 0.07	0.75 ± 0.07
r	-23.0	-10.0	4281	4265 ± 354	-0.53 ± 0.04	-20.28 ± 0.06	0.98 ± 0.09	0.000	0.90 ± 0.08	0.89 ± 0.08
i	-23.0	-11.0	4006	4014 ± 332	-0.46 ± 0.03	-20.63 ± 0.05	1.04 ± 0.09	0.000	1.13 ± 0.11	1.11 ± 0.11
z	-24.0	-12.0	3759	3760 ± 301	-0.40 ± 0.05	-20.87 ± 0.06	1.10 ± 0.07	0.000	1.39 ± 0.13	1.38 ± 0.13

Table 3 shows the number of galaxies and absolute magnitude limits for each sample, along with the parameters of standard Schechter function fits and luminosity densities. Only for blue galaxies in the *u*, *i* and *z* bands does a standard Schechter function provide a statistically acceptable fit to the data at the 2 per cent level or better. For red galaxies, we observe a decline in number density faintwards of the characteristic magnitude M^* with a subsequent increase in faint-end slope at $M_t \sim M^* + 3$. For the red galaxies, and the combined sample, a double-power-law Schechter function (22) is required to fit the shape of the observed LFs. These findings are in apparent agreement with the predictions of halo occupation distribution models, for example, Brown et al. (2008), in which luminous red galaxies are central galaxies, but fainter red galaxies are increasingly more likely to be satellites in relatively massive haloes. An alternative perspective is provided by Peng et al. (2010), who explain the change in faint-end slope of red galaxies via a simple picture for the quenching of star formation by the distinct processes of 'mass quenching' and 'environment quenching'. Our results provide the most precise demonstration of the changing faint-end slope of red galaxies to date.

However, the observed upturn needs to be interpreted with caution, since, from a quick visual inspection, the 164 faint ($^{0.1}M_r - 5\log h > -16$ mag), red galaxies that comprise the upturn include a significant fraction ($\simeq 50$ per cent) of galaxies that appear to be disc like, as well as a number of artefacts. It thus seems likely that dust-reddened disc systems, as well as dwarf galaxies with intrinsically red stellar populations, contribute to the faint-end upturn in the red galaxy LF. Future work will investigate the LF dependence on morphology and dust reddening, utilizing GAMA's multiwavelength coverage.

Double-power-law Schechter function fits are given in Table 4. Likelihood ratio tests show that the double-power-law Schechter function provides significantly better fits than the standard Schechter function for the combined and red galaxy samples,

at least for the redder bands. For the blue galaxies, however, the double-power-law Schechter function fits are actually worse than the standard Schechter function fits when taking into account the two additional degrees of freedom.

The quoted errors need to be treated with caution due to strong correlations between the parameters, particularly in the case of the five-parameter, double-power-law Schechter function fits. Fig. 14 shows 2σ likelihood contours for each pair of parameters from α, M^*, β and M_t for the combined sample. We see that α and β individually are very poorly constrained, with an uncertainty $\Delta\alpha \simeq \Delta\beta \simeq 0.5$. However, the overall faint-end slope $\alpha + \beta$ is very well constrained, with a consistent value in all five pass-bands, $\alpha + \beta = -1.37 \pm 0.05$, for the combined sample. For blue galaxies, $\alpha + \beta = -1.50 \pm 0.03$ and for red galaxies, $\alpha + \beta = -1.6 \pm 0.3$. Consistent faint-end slopes are found for the stellar mass function (Baldry et al. 2011). Also from Fig. 14, we see that the characteristic magnitude M^* is positively correlated with slope α but negatively correlated with β. The transition magnitude M_t is only weakly correlated with either the slope parameter α or the slope parameter β and almost completely uncorrelated with the characteristic magnitude M^*.

Fig. 15 shows 2σ likelihood contours for the red sample. We see that, while still uncertain, the slope parameters α and β are only weakly correlated. The characteristic magnitude M^* is positively correlated with α but almost completely uncorrelated with β. The transition magnitude M_t is strongly anticorrelated with α and virtually independent of β.

Since the shape of the blue galaxy LF is reasonably well fitted by a standard Schechter function, there are huge degeneracies between the double-power-law Schechter function parameters, and so the contour plots contain no useful information, and hence are not shown.

In summary, in analysing the faint end of the LFs, we have found the following:

Table 4. Double-power-law Schechter function fits for low-redshift galaxies. The values for $^{0.1}M_1$, $^{0.1}M_2$ and $N_{\rm gal}$ are the same for each sample as in Table 3. Other columns have the same meaning as the previous table and in addition we tabulate the values of the double-power-law Schechter parameters β and $M_{\rm t}$.

	$N_{\rm pred}$	α	β	$^{0.1}M^* - 5\log h$	$^{0.1}M_{\rm t} - 5\log h$	$\phi^* \times 100$ $/h^3\,{\rm Mpc}^{-3}$	$P_{\rm fit}$	$\rho_{L{\rm fit}}$ $/10^8\,{\rm L}_\odot\,h\,{\rm Mpc}^{-3}$	$\rho_{L{\rm sum}}$
All									
u	9397 ± 761	-0.81 ± 0.26	-0.56 ± 0.28	-17.87 ± 0.14	-17.38 ± 0.39	1.32 ± 0.26	0.005	1.97 ± 0.18	1.97 ± 0.18
g	$11\,199 \pm 798$	0.09 ± 0.10	-1.41 ± 0.10	-19.05 ± 0.05	-18.99 ± 0.06	1.28 ± 0.10	0.000	1.83 ± 0.15	1.83 ± 0.15
r	$12\,900 \pm 968$	0.14 ± 0.09	-1.47 ± 0.09	-19.92 ± 0.10	-19.86 ± 0.18	1.02 ± 0.13	0.011	1.76 ± 0.15	1.76 ± 0.15
i	$10\,447 \pm 759$	0.10 ± 0.01	-1.44 ± 0.03	-20.32 ± 0.04	-20.10 ± 0.12	1.10 ± 0.12	0.606	2.07 ± 0.18	2.07 ± 0.18
z	8664 ± 675	-0.07 ± 0.35	-1.35 ± 0.27	-20.63 ± 0.17	-19.99 ± 0.33	1.28 ± 0.15	0.729	2.41 ± 0.23	2.41 ± 0.23
Blue									
u	6663 ± 508	-1.39 ± 0.03	-0.09 ± 0.02	-18.27 ± 0.05	-17.98 ± 0.37	0.45 ± 0.02	0.015	1.51 ± 0.14	1.52 ± 0.14
g	7610 ± 527	-1.37 ± 0.01	-0.10 ± 0.02	-19.57 ± 0.04	-15.58 ± 4.88	0.42 ± 0.08	0.001	1.12 ± 0.09	1.13 ± 0.10
r	8898 ± 674	-1.40 ± 0.05	-0.09 ± 0.10	-20.28 ± 0.05	-20.14 ± 2.16	0.28 ± 0.03	0.000	0.92 ± 0.09	0.92 ± 0.09
i	6650 ± 468	-1.43 ± 0.06	-0.05 ± 0.09	-20.69 ± 0.05	-19.76 ± 1.47	0.25 ± 0.03	0.225	1.02 ± 0.09	1.02 ± 0.09
z	5081 ± 403	-1.42 ± 0.03	-0.10 ± 0.00	-20.98 ± 0.08	-20.30 ± 0.34	0.22 ± 0.01	0.389	1.10 ± 0.11	1.10 ± 0.11
Red									
u	2845 ± 264	-0.21 ± 0.16	-1.57 ± 0.42	-17.22 ± 0.10	-14.13 ± 0.52	1.34 ± 0.14	0.000	0.53 ± 0.04	0.54 ± 0.04
g	3751 ± 302	-0.14 ± 0.30	-1.28 ± 0.29	-19.08 ± 0.13	-16.39 ± 1.46	1.14 ± 0.17	0.000	0.75 ± 0.07	0.75 ± 0.07
r	4245 ± 349	-0.15 ± 0.29	-1.16 ± 0.10	-19.99 ± 0.15	-17.33 ± 1.17	1.09 ± 0.15	0.001	0.89 ± 0.08	0.89 ± 0.08
i	3974 ± 327	-0.33 ± 0.10	-1.58 ± 0.43	-20.51 ± 0.08	-16.46 ± 0.71	1.12 ± 0.10	0.228	1.13 ± 0.14	1.13 ± 0.14
z	3730 ± 302	-0.27 ± 0.20	-1.51 ± 0.51	-20.75 ± 0.12	-16.93 ± 1.19	1.16 ± 0.09	0.184	1.38 ± 0.16	1.38 ± 0.16

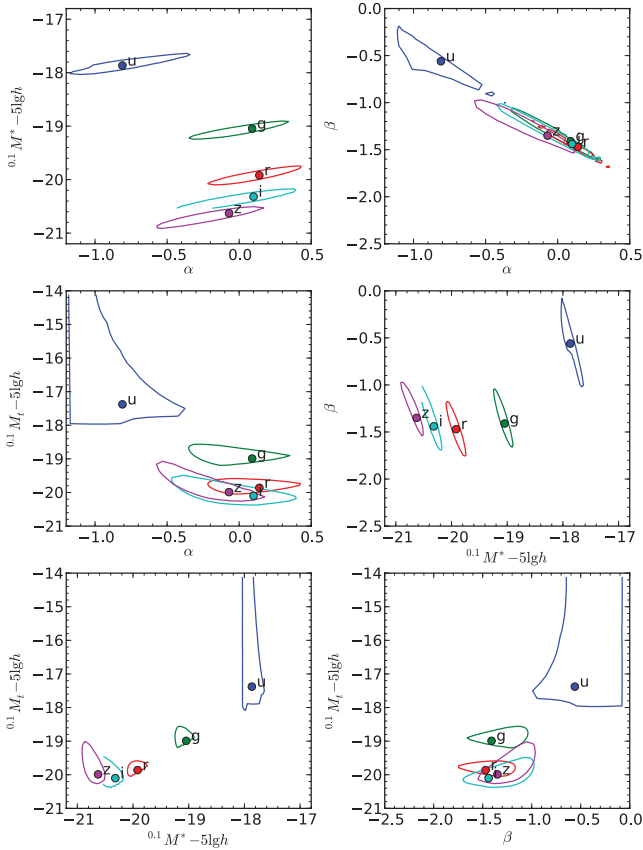**Figure 14.** 2σ likelihood contours for various parameter pairs in double-power-law Schechter function fits to the combined sample for the *ugriz* bands as labelled.
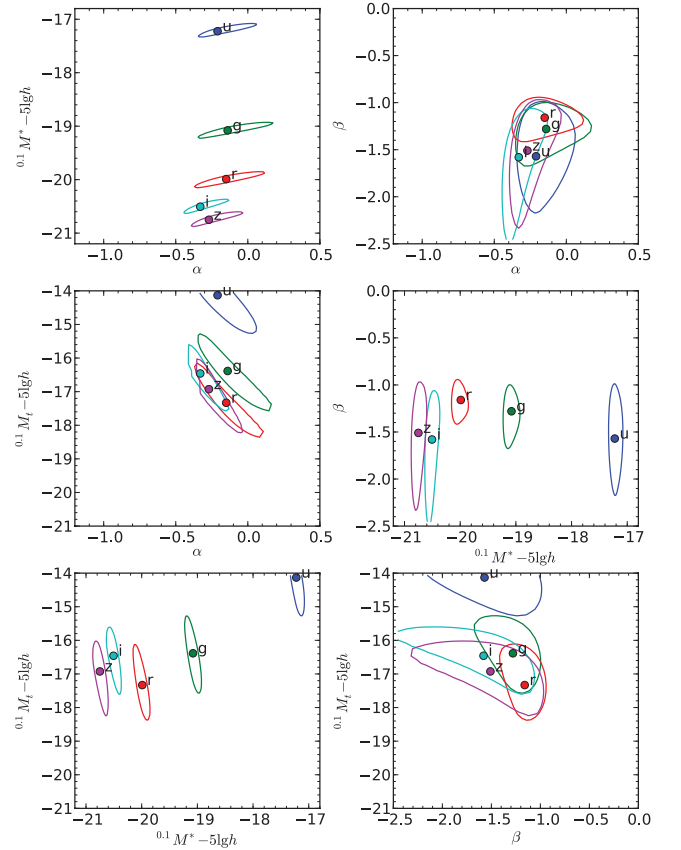
Figure 15. 2σ likelihood contours for various parameter pairs in double-power-law Schechter function fits to the red sample for the *ugriz* bands as labelled.

(i) While a standard Schechter function provides an acceptable fit to the blue galaxy LF in all bands, the red galaxy LF exhibits a decline just faintwards of M^* followed by a pronounced upturn at magnitude $M_t \simeq M^* + 3$. Such an LF is well fitted by a double-power-law Schechter function.

(ii) We caution that the faint end of the red galaxy LF is possibly dominated by dust-reddened systems, rather than by galaxies with intrinsically red stellar populations.

(iii) Neither standard nor double-power-law Schechter function faint-end slopes show any systematic dependence on passband: while strongly colour-dependent, faint-end slopes are largely independent of passband.

(iv) The characteristic magnitude M^* (and to a lesser extent, the transition magnitude M_t) brightens systematically and significantly with passband effective wavelength.

4.4 Luminosity function evolution

We present LFs for the combined, blue and red samples in the *ugriz* bands in four redshift ranges in Fig. 16. Table 5 gives the magnitude limits (chosen to exclude the upturn seen in the LF of red galaxies),[5] observed and predicted numbers of galaxies, and Schechter and evolution parameters in each band. Qualitatively, the *riz* LFs appear to be well fitted by the parametric evolution model, although this model is formally excluded by the likelihood ratio test for almost every colour, band and redshift combination. Even by eye, we see that the evolving Schechter function fits are in extremely poor agreement with the *u*- and *g*-band non-parametric (SWML and $1/V_{max}$) estimates in the highest redshift range, in the sense that the model overpredicts the number density of luminous galaxies by almost an order of magnitude in the *u* band. Equation (5) thus provides a poor fit to the evolution of the *u*- and *g*-band LFs beyond $z \simeq 0.2$ and $z \simeq 0.3$, respectively. It is very possible that the *u*-band flux of more luminous, higher redshift galaxies is being dominated by AGNs. We intend to investigate the LFs of AGN-dominated/star-forming/quiescent galaxies in a future paper.

In addition to the parametric fit, we also fit Schechter functions to the SWML estimates for each redshift slice using least squares. Because the LF faint end is poorly sampled at redshift $z \gtrsim 0.1$, we only fit for all three Schechter parameters, α, M^* and ϕ^*, in the lowest redshift slice. At higher redshifts, we hold α fixed and allow only M^* and ϕ^* to vary. The results of these fits are shown as the dashed lines in Fig. 16 and the insets show 95 per cent likelihood contours of $(M^*, \log \phi^*)$. These least-squares fits are for illustration only. In order to calculate the parameters Q_{SWML} and P_{SWML} given in Table 5, and shown below in Fig. 19, we subdivide into eight redshift bins, perform least-squares fits to the SWML estimates in each, and then fit straight lines to $\log \phi^*$ and M^* versus redshift. We now discuss LF evolution separately, for the *u*, *g* and *riz* bands.

4.4.1 u-band evolution

We observe a gradual brightening of M^* for all samples between $z \simeq 0.05$ and $z \simeq 0.15$, and already a bright-end excess above a Schechter function is becoming apparent. By $z \simeq 0.25$, the evolving model provides a very poor fit to the non-parametric estimates: the former is much steeper than the latter, and by $z \simeq 0.4$ the parametric fit overpredicts the number density of galaxies by almost an order

of magnitude. From the least-squares fits to the non-parametric estimates, we see a dramatic brightening of M^* in the highest redshift range (there are too few red galaxies to obtain a sensible LF fit in this bin). This is due to the very shallow slope at the bright end of the LF, leading the Schechter fit to prefer brightening M^* to increasing ϕ^*. In reality, we suspect that this shallow slope is caused by an increasing fraction of highly-luminous AGNs, rather than by such strong luminosity evolution in non-active galaxies. An alternative explanation is that photometric errors in the *u* band are manifesting themselves as unrealistically strong luminosity evolution. This possibility will explored when VST-KIDS data become available in the GAMA regions.

4.4.2 g-band evolution

The parametric model provides a good fit out to redshift $z \simeq 0.2$, beyond which a bright-end excess results in an overprediction of the LF relative to the non-parametric estimates. From these latter estimates, one sees that the number density of blue galaxies is gradually increasing with redshift, whereas red galaxies show the opposite trend. Photometric errors are less likely to be a problem in the *g* than in the *u* band, and so again we suspect that AGNs are dominating the bright end of the LF at higher redshifts. This interpretation does not necessarily imply rapid evolution of the AGN population – the volume sampled at low redshifts is simply too small to detect them in significant numbers.

4.4.3 riz-band evolution

Evolution in the *r*, *i* and *z* bands is qualitatively very similar, and so we discuss them together. The parametric model provides a reasonable fit in all redshift slices, although it should be said that the formal fit probabilities from the likelihood ratio test are mostly below 1 per cent. This does not necessarily mean that the model is a poor fit, as we see from simulations (Appendix A) that the non-parametric LF estimates are biased when the underlying LF is evolving. The likelihood ratio test provides improved probabilities when we consider narrower ranges in redshift. From the non-parametric fits, we see that M^* brightens with redshift for all samples. At low redshifts, red galaxies have a much higher space density than blue, but as redshift increases, the density of red galaxies drops and that of blue galaxies increases, until blue galaxies come to dominate by redshifts $z \simeq 0.4$.

4.4.4 Comparison with previous results

We compare our evolving LFs with previous estimates in Fig. 17. Here we plot the LFs in three redshift ranges (0.002, 0.2], (0.2, 0.4] and (0.4, 0.6]. We choose these ranges to coincide with the first three redshift bins used by Ilbert et al. (2005) in their analysis of the VIMOS-VLT Deep Survey (VVDS). Following these authors, we assume approximate correspondence between the rest-frame *BVRI* and the $^{0.1}griz$ passbands, and assume that $^{0.0}M_U^* = {}^{0.1}M_u^* - 0.25$. Their LFs are shown as the red lines: solid over the magnitude range actually fitted, dashed where extrapolated.

In the low-redshift range (top row), we also show the non-parametric LF estimates of SDSS galaxies from Blanton et al. (2003b) as the blue lines. Their estimates are in good agreement with our non-parametric SWML and $1/V_{max}$ estimates except that we see a slightly higher density of luminous galaxies, particularly in the *g* band ($^{0.1}M_g - 5 \log h \lesssim -21$ mag). This difference is likely

---

[5] This choice of magnitude limits also corresponds closely to those of Blanton et al. (2003b).
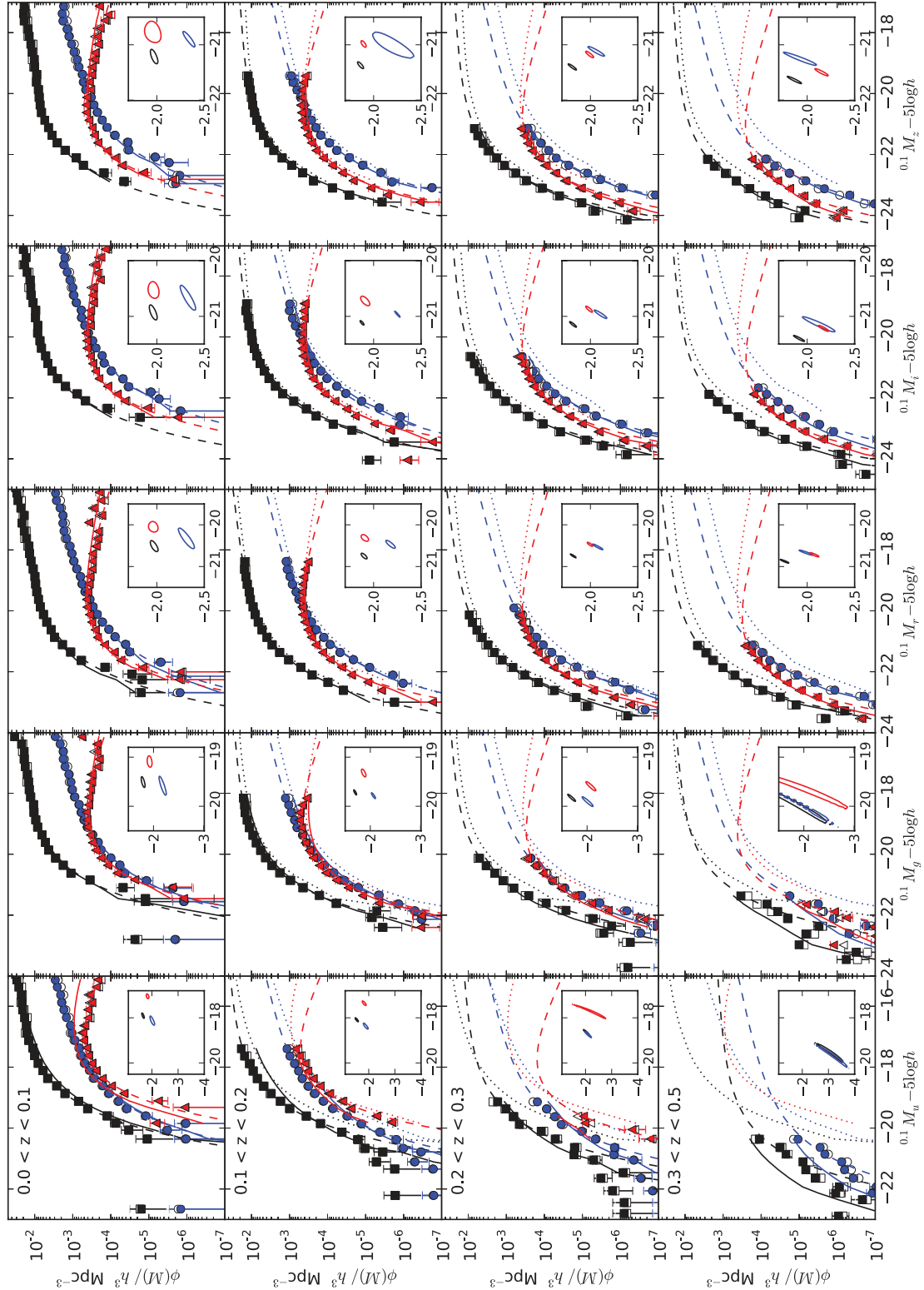
Figure 16. Evolution of the *ugriz* LFs. The five columns show the *ugriz* LFs, respectively, from the left-hand to right-hand side. The four rows show the LFs in four redshift ranges increasing from the top to bottom as indicated in the leftmost panels. The filled black squares show SWML estimates for combined red and blue samples, and the filled blue circles and red triangles show SWML LFs for the blue and red samples, respectively. The open symbols show the corresponding $1/V_{\mathrm{max}}$ estimates – in most cases these are indistinguishable from the SWML estimates. The continuous lines show the parametric evolving LF for each sample The dotted lines reproduce the parametric LF fit for each sample from the lowest redshift bin. The dashed lines show least-squares fits to the SWML estimates with α fixed at higher redshifts. The insets show the 95 per cent likelihood contours for $(M^*, \log \phi^*)$ parameters obtained from these fits. LFs (but not contours) for the blue and red samples have been scaled by a factor of 0.1 to aid legibility.

Table 5. Evolving Schechter function fits to *ugriz* LFs. The columns are the same as in Table 3, with the addition of the evolution parameters Q_{par} and P_{par} determined from the parametric model, and Q_{SWML} and P_{SWML} determined from least-squares fits to SWML estimates in eight redshift slices as described in the text.

|	$^{0.1}M_1$ $^{0.1}M_2$ $-5\log h$	N_{gal}	N_{pred}	α	$^{0.1}M^* - 5\log h$	Q_{par}	P_{par}	Q_{SWML}	P_{SWML}	$\phi^* \times 100$ /h^3 Mpc^{-3}
All										
u	-23.0 -15.0	21 120	$13\,616 \pm 1941$	-1.10 ± 0.08	-17.98 ± 0.08	6.2 ± 0.5	-8.5 ± 1.2	4.6 ± 0.7	-1.1 ± 0.4	3.10 ± 0.53
g	-24.0 -16.0	37 245	$31\,909 \pm 2876$	-1.10 ± 0.02	-19.58 ± 0.03	2.9 ± 0.5	-1.5 ± 1.1	0.2 ± 0.5	2.1 ± 0.4	1.80 ± 0.22
r	-24.0 -16.0	90 554	$87\,163 \pm 5494$	-1.23 ± 0.01	-20.70 ± 0.04	0.7 ± 0.2	1.8 ± 0.5	0.2 ± 0.2	1.6 ± 0.2	0.94 ± 0.10
i	-25.0 -17.0	66 069	$57\,351 \pm 3290$	-1.12 ± 0.02	-20.97 ± 0.03	1.5 ± 0.1	0.0 ± 0.4	0.6 ± 0.2	1.2 ± 0.2	1.16 ± 0.15
z	-25.0 -17.0	51 657	$44\,771 \pm 2803$	-1.07 ± 0.02	-21.22 ± 0.04	1.7 ± 0.3	-0.5 ± 0.8	0.8 ± 0.2	1.3 ± 0.2	1.26 ± 0.18
Blue										
u	-23.0 -15.0	15 205	$10\,508 \pm 1214$	-1.43 ± 0.07	-18.28 ± 0.10	5.5 ± 0.6	-7.1 ± 1.5	3.5 ± 0.8	-0.2 ± 0.6	1.31 ± 0.25
g	-24.0 -16.0	21 035	$16\,733 \pm 2637$	-1.40 ± 0.03	-19.60 ± 0.06	3.1 ± 0.7	-1.2 ± 1.5	0.4 ± 0.8	2.1 ± 0.6	0.73 ± 0.03
r	-24.0 -16.0	43 222	$39\,901 \pm 1993$	-1.49 ± 0.03	-20.45 ± 0.06	0.8 ± 0.3	2.9 ± 0.6	0.6 ± 0.3	1.4 ± 0.2	0.38 ± 0.05
i	-25.0 -17.0	26 845	$22\,313 \pm 1608$	-1.45 ± 0.02	-20.76 ± 0.06	1.7 ± 0.4	1.2 ± 0.9	0.8 ± 0.4	1.5 ± 0.3	0.42 ± 0.06
z	-25.0 -17.0	18 588	$17\,993 \pm 855$	-1.45 ± 0.03	-21.03 ± 0.04	0.9 ± 0.2	3.6 ± 0.5	0.8 ± 0.4	2.0 ± 0.4	0.34 ± 0.04
Red										
u	-23.0 -15.0	5915	9488 ± 2179	-0.14 ± 0.13	-17.32 ± 0.07	6.4 ± 1.4	-8.1 ± 3.4	5.5 ± 0.9	-1.2 ± 0.7	4.28 ± 1.44
g	-24.0 -16.0	16 210	$11\,685 \pm 2696$	-0.43 ± 0.05	-19.30 ± 0.06	3.6 ± 1.4	-3.9 ± 2.8	2.8 ± 0.6	-0.4 ± 0.4	1.26 ± 0.17
r	-24.0 -16.0	47 332	$42\,882 \pm 2426$	-0.57 ± 0.02	-20.34 ± 0.03	1.8 ± 0.1	-1.2 ± 0.5	1.7 ± 0.2	-0.1 ± 0.2	1.11 ± 0.15
i	-25.0 -17.0	39 224	$33\,962 \pm 1840$	-0.54 ± 0.03	-20.73 ± 0.03	2.0 ± 0.1	-1.8 ± 0.5	2.3 ± 0.2	-0.5 ± 0.2	1.16 ± 0.15
z	-25.0 -17.0	33 069	$27\,543 \pm 1701$	-0.49 ± 0.05	-20.97 ± 0.06	2.4 ± 0.3	-2.7 ± 0.7	2.7 ± 0.2	-1.0 ± 0.2	1.32 ± 0.16
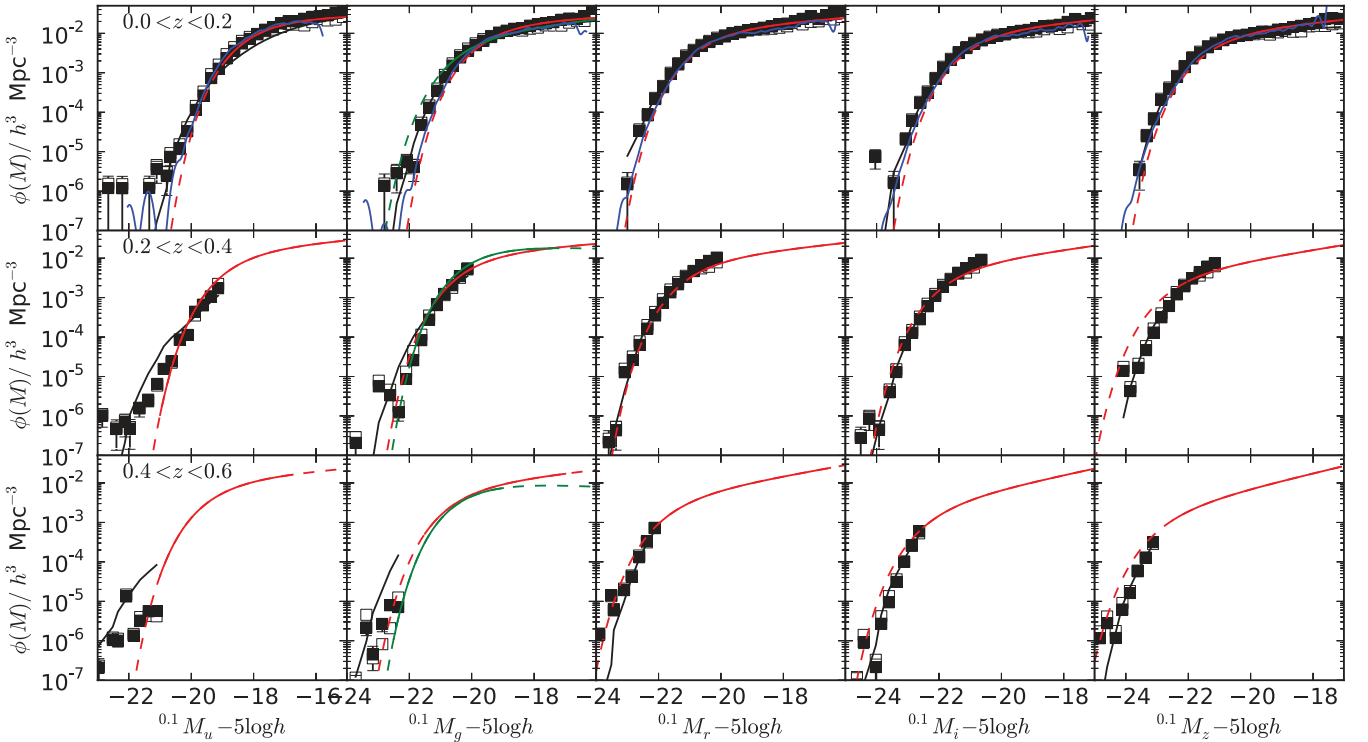
Figure 17. Comparison of our *ugriz* LFs for the combined sample in three redshift ranges as indicated with previous estimates. The filled and open symbols and black lines show our SWML, $1/V_{max}$ and parametric fits, respectively. The blue lines (upper panels only) show the $z \simeq 0.1$ SDSS LFs estimated by Blanton et al. (2003b). The red lines show the VVDS LFs in the bands *UBVRI*, respectively, from Ilbert et al. (2005). The green lines show the zCOSMOS *B*-band LFs from fig. 1 of Zucca et al. 2009. The VVDS and zCOSMOS fits are shown as the solid lines over the magnitude range actually fitted; the dashed lines show extrapolations outside the fitted magnitude range.

to be due to the greater depth of the GAMA sample compared with the SDSS: the mean redshift in this range is $\bar{z} = 0.13$ for GAMA versus $\bar{z} = 0.10$ for the SDSS. The GAMA sample thus contains a higher fraction of more distant and hence more evolved galaxies.

The VVDS Schechter fits in the lowest redshift bin show a slightly lower density of luminous galaxies than seen in GAMA and the SDSS. Note, however, that the bright end of the low-redshift LF is very poorly constrained by Ilbert et al. due to their bright apparent

magnitude limit of $I_{AB} = 17.5$. The zCOSMOS *B*-band LF from fig. 1 of Zucca et al. (2009) (Zucca, private communication; green line) shows a bright-end excess relative to GAMA and to the VVDS. While reaching about 1.5 mag brighter than the VVDS, the zCOS-MOS low-redshift LF still relies on extrapolation at magnitudes brighter than $M_B - 5 \log h = -21$ mag.

At intermediate redshifts (middle row), our LFs are in good agreement with the VVDS and zCOSMOS apart from an excess of *u*-bright galaxies in GAMA and, conversely, a much higher bright-end fit by the VVDS in the $I\,(^{0.1}z)$ band. The latter discrepancy is almost certainly due to poor coverage of the bright end of the *I*-band LF at redshifts $0.2 < z < 0.4$ by the VVDS.

In the highest redshift range (bottom row), the extrapolation of the VVDS Schechter fit shows a higher abundance of luminous galaxies in the redder *VRI* bands than GAMA. In this redshift range, the comparison is not quite fair, since GAMA contains very few galaxies beyond $z = 0.5$, and so much of the VVDS excess is likely to be due to galaxies in the redshift range $0.5 < z < 0.6$.

Overall, our evolving LF estimates are in reasonable agreement with the previous results of Blanton et al. (2003b), Ilbert et al. (2005) and Zucca et al. (2009).

4.4.5 Schechter parameter likelihood contours

2σ likelihood contours for the Schechter parameters (α, M^*), determined using the parametric fits, are shown in Fig. 18. For the combined sample, we find roughly consistent faint-end slopes $\alpha = -1.1 \pm 0.1$ in all bands. The slightly steeper slope seen in the *r* band is most likely due to the fact that GAMA is selected in the *r* band, and hence we probe slightly further down the LF in this than the surrounding bands. Similarly, the slightly steeper slopes in our fits to the low-redshift sample (Table 3) are due to the inclusion of fainter-magnitude galaxies in those fits. As expected, M^* increases systematically in brightness with increasing wavelength from *u* to *z*. Red galaxies have systematically shallower faint-end slopes ($\alpha \simeq -0.5$ in *griz*) than blue galaxies ($\alpha = -1.45 \pm 0.05$) in all bands. The characteristic magnitudes M^* are fainter for red galaxies than for blue in the *ugr* bands and are comparable in the *iz* bands.

Fig. 18 also shows Schechter function parameters estimated from the SDSS main galaxy sample by Blanton et al. (2003b). We find systematically steeper faint-end slopes (apart from in the *z* band) and brighter characteristic magnitudes (apart from the *u* band). Since our non-parametric estimates are in good agreement (Fig. 17), these differences most likely arise due to strong degeneracies between the parameters α, M^* and Q: (α, M^*), (α, Q) and (M^*, Q) are all positively correlated.

4.4.6 Evolution parameter likelihood contours

In Fig. 19, we show 2σ likelihood contours for the luminosity evolution parameters Q and P from our parametric fits, along with estimates of these quantities and their errors from least-squares fits of Schechter functions to the SWML estimates made in eight redshift ranges. The differences between the estimates of these parameters are frequently larger than the formal errors associated with each method. This indicates that our assumption of linear evolution of M^* and $\log \phi^*$ with redshift is only approximate.

For the combined sample, luminosity evolution is least in the *r* band ($Q_{par} \simeq 0.7$), increasing to $Q_{par} \simeq 1.6$ in the *i* and *z* bands. Luminosity evolution is even more pronounced in the *g* and *u* bands ($Q_{par} \simeq 2.9$ and 6.2, respectively), although, as previously noted,
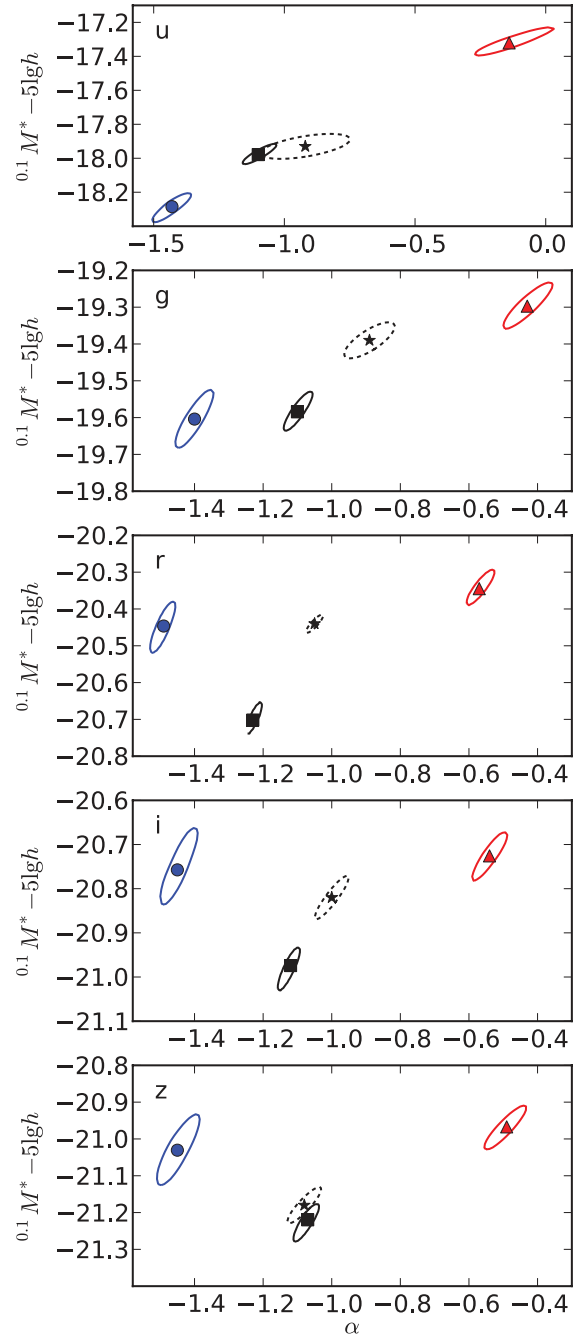

Figure 18. 2σ likelihood contours for the evolving Schechter function parameters α and M^* in the *ugriz* bands for combined, blue and red samples (black, blue and red contours, respectively). The asterisks and dotted ellipses show the best-fitting values and 2σ error ellipses on the parameters reported by Blanton et al. (2003b) (combined colours only), respectively.

the parametric model performs very poorly in these bands, and so these values are unreliable at best. Luminosity evolution is more pronounced for the red galaxy population than the blue.

Blue galaxies exhibit positive density evolution ($P_{par} > 0$ in all bands apart from *u* and *g*, $P_{SWML} > 0$ in all bands apart from *u*), whereas red galaxies show negative density evolution; both P_{par} and P_{SWML} are negative in all bands. This observation is in good qualitative agreement with an analysis of the zCOSMOS by Zucca et al. (2009), who find that both early- and late-spectroscopic-
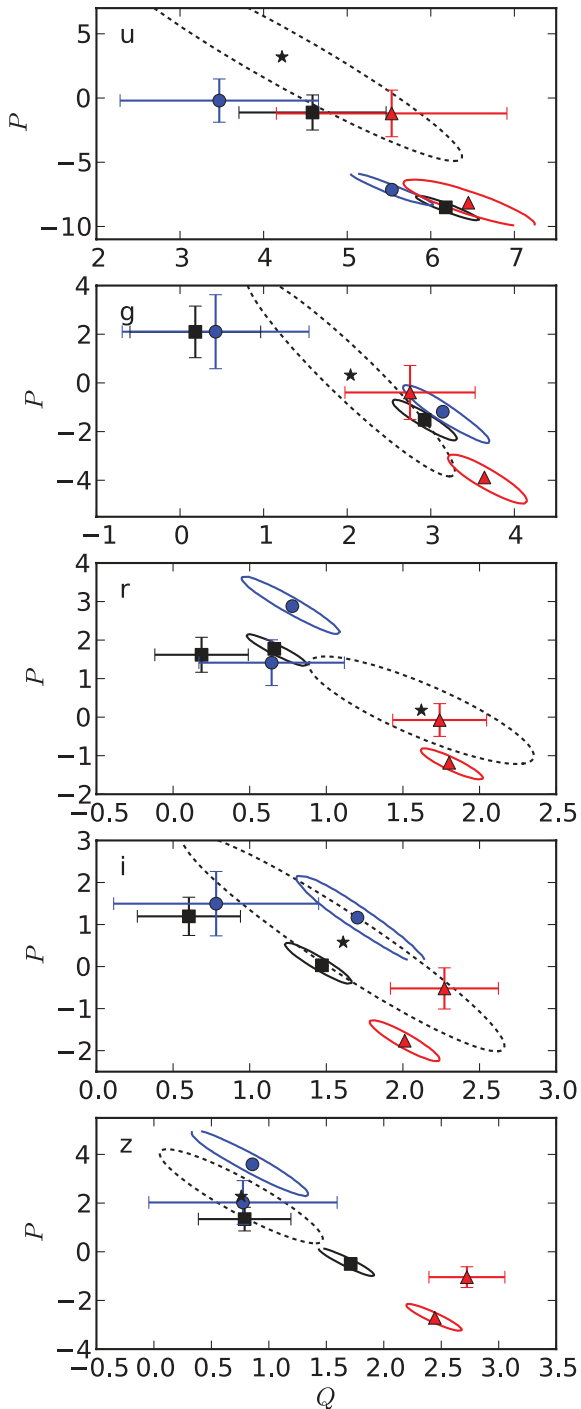
Figure 19. 2σ likelihood contours for the evolving Schechter function parameters Q and P in the *ugriz* bands for combined, blue and red samples (black, blue and red contours, respectively). The error bars with symbols show evolution parameters and their 2σ errors determined from a least-squares fit to SWML estimates of the LF in eight redshift ranges covering $0.002 < z < 0.5$. The asterisks and dotted ellipses show the best-fitting values and 2σ error ellipses on the parameters reported by Blanton et al. (2003b) (combined colours only), respectively.

type galaxies brighten in M^* by $\simeq 0.5$ mag over the redshift range $z \simeq 0.2$ to $z \simeq 0.9$, but that ϕ^* for early types decreases by a factor of $\simeq 1.7$ over the same redshift range; for late types, ϕ^* increases by a factor of $\simeq 1.8$.

Density evolution for the combined sample is positive in the *r* band; in other bands, *P* is either negative or consistent with zero, compensating for the stronger luminosity evolution in these bands. Thus, the contrary density evolution of blue and red galaxies largely cancels out in the combined sample. For all bands and samples, the evolution parameters (Q, P) are strongly anticorrelated. We remind the reader that the maximum-likelihood luminosity evolution $Q_{\rm par}$ is determined along with α and M^*, independently of the normalization of the LF. Density evolution $P_{\rm par}$ does depend on the fitted value of $Q_{\rm par}$, as well as the Schechter parameters, resulting in the observed anticorrelation between Q and P. In the redder bands, *riz*, the combined LD evolution $P + Q$ is stronger for blue galaxies, $(P + Q)_{\rm par} \simeq 3.7 \pm 0.8$, than for red, $(P + Q)_{\rm par} \simeq 0.2 \pm 0.5$.

Fig. 19 also shows evolution parameters determined from the SDSS main galaxy sample by Blanton et al. (2003b). The 2σ likelihood contours intersect in *gri*, and narrowly miss in *u* and *z*. In the *r* band, we find weaker luminosity evolution and a compensating stronger density evolution, and vice versa in *z*. Our least-squares fits to the SWML estimates in the *u* band yield comparable *Q* estimates to Blanton et al. (2003b). Their density evolution, unlike ours, is positive, but has a very large error.

Although sampling a smaller volume, the GAMA data analysed here have a mean redshift $\bar{z} \simeq 0.2$ compared with $\bar{z} \simeq 0.1$ for the data analysed by Blanton et al. We thus have a longer redshift baseline over which to measure evolution.

Hopkins (2004), in an analysis combining constraints from the star formation rate density of the Universe and 1.4-GHz radio source counts, found $Q = 2.70 \pm 0.60$ and $P = 0.15 \pm 0.60$ for the star-forming galaxy population.[6] This measurement, sensitive to the star-forming population up to $z \simeq 1$, is consistent with our parametric fit results for blue galaxies in the *g* band at the low-redshift end of this range. However, given the very large discrepancy between $Q_{\rm par}$ and $Q_{\rm SWML}$ for blue galaxies in the *g* band, the apparent agreement may be fortuitous.

For red galaxies, Brown et al. (2007) find that M^* in the *B* band brightens by $\simeq -0.7$ mag from redshift $z = 0.2$ to 1, while ϕ^* declines by about 25 per cent, in qualitative agreement with our results.

4.4.7 Evolution summary

To summarize our findings regarding the evolution of the LF:

(i) The evolutionary model (equation 5) provides a reasonable fit in the redder bands, *riz*, but performs poorly in the *u* and *g* bands, overpredicting the LF of luminous galaxies at high redshift. This is possibly due to a significant contribution from AGNs.

(ii) Our non-parametric LF estimates are in good agreement with SDSS measurements at low redshift and with results from the VVDS and zCOSMOS at higher redshifts, over magnitude ranges where our LF estimates overlap.

(iii) There is a strong degeneracy between the luminosity and density evolution parameters Q and P. One should be wary in using them in isolation, for example, using the Q parameter to apply evolutionary corrections.

(iv) Nevertheless, red galaxies in all bands show evidence for positive luminosity evolution $(Q > 0)$ and negative density evolution $(P < 0)$.

---

[6] Note that Hopkins actually models evolution as $L \propto (1 + z)^Q$ and $\phi \propto (1 + z)^P$.

(v) Blue galaxies show less luminosity evolution but show evidence for positive density evolution.

(vi) The observation of decreasing number density of blue galaxies but increasing number density of red galaxies with cosmic time implies that the transition from blue cloud to red sequence is an important and ongoing phenomenon since redshifts $z \simeq 0.5$.

(vii) The combined luminosity plus density evolution is stronger for blue than for red galaxies.

4.5 Luminosity density evolution

As we have seen in the previous section, while it can be difficult to isolate the effects of luminosity and density evolution, evolution in LD is better constrained. Fig. 20 shows the LD $\rho_{L\text{sum}}$ measured in eight redshift bins up to $z = 0.5$, according to equation (16), along with the prediction $\rho_{L\text{fit}}$ of the parametric model (equation 14). These results are tabulated in Table 6. For the combined sample, in all bands other than u, we see LD increasing with redshift, steeply between redshifts $z = 0$ and $z \simeq 0.15$, slightly more gradually thereafter. The blue galaxy LD increases more steeply with redshift than the combined sample. The LD of red galaxies barely evolves with redshift beyond $z \simeq 0.15$; thus, the relative contribution to LD from blue galaxies comes to dominate by redshifts $z \simeq 0.2$. Given our choice of colour cut (equation 3), red and blue galaxies contribute roughly equally to the LD in the r and i bands at low redshifts ($z \lesssim 0.15$); red galaxies are slightly dominant in the z band but under-represented in the u and g bands.

Fig. 20 also shows the LD estimated from the SDSS by Blanton et al. (2003b) and Montero-Dorta & Prada (2009) at a mean redshift of $z \simeq 0.1$. Our results are in excellent agreement with those of Blanton et al. (2003b). Montero-Dorta & Prada (2009) appear to have significantly underestimated the g-band LD, although their estimates in other bands are in agreement with ours and those of Blanton et al. (2003b). The open triangles show LD estimates from CNOC2. We have taken the $q_0 = 0.1$ 'Total' values from table 3 of Lin et al. 1999 in the U, B and R bands, corresponding roughly to $^{0.1}u - 0.25$, $^{0.1}g$ and $^{0.1}i$, respectively. We convert the CNOC2 luminosity densities from physical units of $h\,\text{W}\,\text{Hz}^{-1}\,\text{Mpc}^{-3}$ into AB magnitudes using $M_{\text{AB}} = 34.1 - 2.5 \log \rho_L$ and then convert into solar luminosities using the assumed absolute magnitudes of the Sun quoted in Section 3.2. The B- and R-band LD estimates are in reasonable agreement with our g- and i-band estimates, while the CNOC2 U-band LD is many times larger than our u-band LD at redshifts $z \gtrsim 0.15$. The open diamonds show u-band LD estimates from Prescott et al. (2009).

Note that our u- and g-band LD estimates will be adversely affected by the poor fit of the parametric model for LF evolution. The selection function in the denominator of equation (16) will be overestimated at high redshifts in these bands, and hence the summed LD itself will be underestimated, leading to the decline in LD with redshift seen for the u band in Fig. 20.

Previous studies of LD evolution (e.g. Lilly et al. 1996; Lin et al. 1999; Bell et al. 2004; Baldry et al. 2005; Willmer et al. 2006; Faber et al. 2007; Prescott et al. 2009) have found that for blue and non-colour-selected galaxies, ρ_L increases monotonically with redshift, while for red galaxies, it is approximately constant, with a possible decline beyond redshift $z \simeq 1$. We have presented the most detailed investigation to date of LD evolution since redshift $z \simeq 0.5$, finding consistent results in the gri and z bands with previous analyses which have focused primarily on evolution beyond redshifts $z \simeq 0.5$.
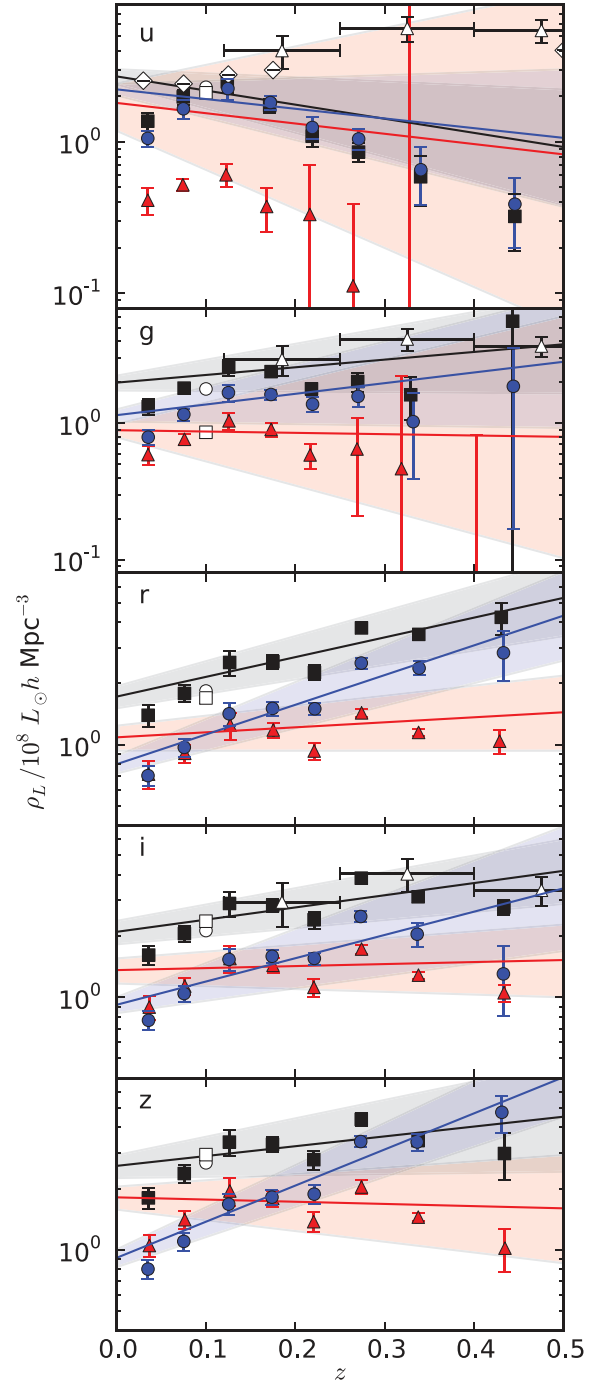

Figure 20. Luminosity density in the five bands $ugriz$ labelled as a function of redshift. The points with error bars show the LD estimated by summing galaxies in each luminosity range (equation 16). The lines show the predictions from the parametric fits (equation 14) and shaded regions show confidence limits obtained by combining the lower and upper 1σ limits on $\rho_L(0)$, Q and P. The black squares, blue circles and red triangles show results for the combined, blue and red samples, respectively. The open circles and squares show the LD estimated at redshift $z \simeq 0.1$ from SDSS data by Blanton et al. (2003b) and Montero-Dorta & Prada (2009), respectively. The open triangles show LD estimates from CNOC2 (table 3 of Lin et al. 1999) in the U, B and R bands corresponding roughly to $^{0.1}u - 0.25$, $^{0.1}g$ and $^{0.1}i$, respectively. The diamonds show u-band LD estimates from Prescott, Baldry & James (2009).

Table 6. Luminosity density evolution. The column labelled 'Fit' gives the redshift-zero LD from the parametric fit (equation 15) and subsequent columns show the LD obtained from summing over galaxies (equation 16) in the indicated redshift ranges. Units are $10^8\,L_\odot\,h\,Mpc^{-3}$.

Redshift	Fit	0.0–0.05	0.05–0.1	0.1–0.15	0.15–0.2	0.2–0.25	0.25–0.3	0.3–0.4	0.4–0.5
All									
u	2.70 ± 0.31	1.37 ± 0.19	1.98 ± 0.22	2.49 ± 0.38	1.73 ± 0.17	1.09 ± 0.17	0.86 ± 0.12	0.59 ± 0.21	0.32 ± 0.13
g	1.99 ± 0.25	1.33 ± 0.17	1.81 ± 0.17	2.58 ± 0.36	2.39 ± 0.21	1.79 ± 0.16	2.02 ± 0.32	1.62 ± 0.56	5.61 ± 8.27
r	1.72 ± 0.21	1.40 ± 0.18	1.79 ± 0.17	2.54 ± 0.36	2.56 ± 0.20	2.26 ± 0.19	3.75 ± 0.17	3.49 ± 0.14	4.23 ± 0.76
i	2.10 ± 0.28	1.61 ± 0.18	2.06 ± 0.20	2.89 ± 0.41	2.82 ± 0.20	2.40 ± 0.23	3.86 ± 0.18	3.12 ± 0.15	2.78 ± 0.24
z	2.59 ± 0.33	1.80 ± 0.21	2.37 ± 0.24	3.39 ± 0.48	3.30 ± 0.27	2.78 ± 0.30	4.38 ± 0.33	3.45 ± 0.18	2.98 ± 0.76
Blue									
u	2.22 ± 0.20	1.05 ± 0.12	1.65 ± 0.23	2.25 ± 0.35	1.82 ± 0.20	1.24 ± 0.21	1.04 ± 0.17	0.65 ± 0.27	0.39 ± 0.19
g	1.15 ± 0.12	0.79 ± 0.10	1.16 ± 0.12	1.68 ± 0.24	1.63 ± 0.14	1.38 ± 0.17	1.58 ± 0.26	1.03 ± 0.64	1.87 ± 1.70
r	0.80 ± 0.08	0.70 ± 0.08	0.97 ± 0.10	1.42 ± 0.19	1.51 ± 0.12	1.50 ± 0.10	2.52 ± 0.15	2.38 ± 0.19	2.83 ± 0.78
i	0.92 ± 0.08	0.77 ± 0.08	1.04 ± 0.09	1.53 ± 0.19	1.59 ± 0.12	1.55 ± 0.11	2.50 ± 0.16	2.04 ± 0.27	1.30 ± 0.49
z	0.91 ± 0.09	0.80 ± 0.09	1.10 ± 0.11	1.68 ± 0.20	1.82 ± 0.15	1.88 ± 0.19	3.41 ± 0.22	3.39 ± 0.32	4.75 ± 0.97
Red									
u	1.81 ± 0.62	0.41 ± 0.08	0.52 ± 0.05	0.61 ± 0.10	0.37 ± 0.12	0.33 ± 0.37	0.11 ± 0.28	–	–
g	0.89 ± 0.10	0.59 ± 0.10	0.76 ± 0.07	1.04 ± 0.15	0.90 ± 0.11	0.59 ± 0.13	0.65 ± 0.44	0.46 ± 1.77	0.05 ± 0.77
r	1.09 ± 0.15	0.72 ± 0.11	0.91 ± 0.09	1.25 ± 0.19	1.18 ± 0.10	0.93 ± 0.09	1.43 ± 0.06	1.15 ± 0.05	1.04 ± 0.14
i	1.36 ± 0.19	0.89 ± 0.12	1.13 ± 0.11	1.55 ± 0.24	1.44 ± 0.12	1.12 ± 0.11	1.73 ± 0.09	1.28 ± 0.05	1.05 ± 0.10
z	1.81 ± 0.23	1.05 ± 0.13	1.41 ± 0.14	1.95 ± 0.30	1.79 ± 0.16	1.38 ± 0.15	2.04 ± 0.16	1.45 ± 0.06	1.02 ± 0.25

5 CONCLUSIONS

We have presented the first measurements of the *ugriz* galaxy LFs from the GAMA survey, after correcting for imaging, target and spectroscopic incompleteness. At low redshift ($z < 0.1$), the shapes of the blue galaxy LFs are reasonably matched, albeit not in detail, by standard Schechter functions. LFs for red galaxies show a notable dip at intermediate magnitudes, requiring double-power-law Schechter functions to obtain an adequate fit. One should be cautious in interpreting this as the upturn predicted by halo occupation distribution models (e.g. Brown et al. 2008) and the Peng et al. (2010) quenching model, since the faint end of our red galaxy LF contains a significant fraction of edge-on disc systems, which are likely to be dust-reddened. We find consistent faint-end slopes in all bands, $\alpha + \beta = -1.35 \pm 0.05$ for the combined sample.

In order to determine the evolution of the LF, we employ the parametric model of Lin et al. (1999) in which characteristic magnitude M^* and log density $\log \phi^*$ are allowed to vary linearly with redshift. We test the parametric model by comparing with estimates using the $1/V_{max}$ and SWML estimates. We find that the r, i and z bands are qualitatively well fitted by this model, although the model provides poor likelihood fits compared with the SWML. The model predicts an excessively high number density in the u and g bands at high redshift, most likely due to QSO/Seyfert contamination (Montero-Dorta & Prada 2009). With this caveat in mind, we find positive (i.e. increasing with redshift) luminosity evolution in all bands and for all colour samples. Luminosity evolution is stronger for red than for blue galaxies, with blue galaxies brightening by $\simeq$1–1.5 mag per unit redshift and red galaxies brightening by $\simeq$2–2.5 mag per unit redshift.

Number density evolution for blue galaxies is positive in the redder *riz* bands in which it can be reliably measured, while red galaxies exhibit negative density evolution. This observation of decreasing number density of blue galaxies but increasing number density of red galaxies with cosmic time implies that the transition from blue cloud to red sequence is an important and ongoing phenomenon since redshifts $z \simeq 0.5$. Investigation of the mechanism that causes this transition will be the subject of future work, but it appears un-

likely that mergers play a dominant role at these moderate redshifts, given the low merger fraction ($\sim$5 per cent or less) observed at low redshift by for example, Conselice, Yang & Bluck (2009) and Lotz et al. (2011).

Luminosity density increases from redshift zero until $z \simeq 0.15$, beyond which redshift it increases more gradually for the combined sample. The LD of red galaxies is roughly constant beyond $z \simeq 0.15$, whereas that for blue galaxies keeps on increasing, leading to blue galaxies dominating the LD at higher redshifts.

In this paper, we have not considered the effects of internal dust extinction on the LF, nor have we considered the effects of using total as opposed to Petrosian magnitudes (Graham et al. 2005; Hill et al. 2011). These extensions to the analysis will be considered in a future paper, along with a measurement of the galaxy LF for AGN-dominated, star-forming and quiescent galaxies which, it is hoped, will resolve the problems encountered while attempting to fit an evolutionary model in the u and g bands.

REFERENCES

Abazajian K. et al., 2003, AJ, 126, 2081
Abazajian K. et al., 2004, AJ, 128, 502
Abazajian K. et al., 2009, ApJS, 182, 543
Adelman-McCarthy J. K. et al., 2008, ApJS, 175, 297
Baldry I. K., Glazebrook K., Brinkmann J., Ivezić Ž., Lupton R. H., Nichol R. C., Szalay A. S., 2004, ApJ, 600, 681
Baldry I. K. et al., 2005, MNRAS, 358, 441
Baldry I. K., Glazebrook K., Driver S. P., 2008, MNRAS, 388, 945
Baldry I. K. et al., 2010, MNRAS, 404, 86
Baldry I. K. et al., 2011, MNRAS, in press
Bell E. F. et al., 2004, ApJ, 608, 752
Benson A. J. Bower R. G., Frenk C. S., Lacey C. G., Baugh C. M., Cole S., 2003, ApJ, 599, 38
Blanton M. R., Roweis S., 2007, AJ, 133, 734
Blanton M. R. et al., 2001, AJ, 121, 2358
Blanton M. R. et al., 2003a, AJ, 125, 2348
Blanton M. R. et al., 2003b, ApJ, 592, 819
Blanton M. R. et al., 2005a, AJ, 129, 2562
Blanton M. R., Lupton R. H., Schlegel D. J., Strauss M. A., Brinkmann J., Fukugita M., Loveday J., 2005b, ApJ, 631, 208
Brough S. et al., 2011, MNRAS, 413, 1236
Brown M. J. I., Dey A., Jannuzi B. T., Brand K., Benson A. J., Brodwin M., Croton D. J., Eisenhardt P. R., 2007, ApJ, 654, 858
Brown M. J. I. et al., 2008, ApJ, 682, 937
Cameron E., Driver S. P., 2007, MNRAS, 377, 523
Cameron E., Driver S. P., 2009, A&A, 493, 489
Christodoulou L. et al., 2011, MNRAS, submitted
Cole S., 2011, MNRAS, 416, 739
Cole S., Lacey C., Baugh C., Frenk C., 2000, MNRAS, 319, 168
Conselice C. J., Yang C., Bluck A. F. L., 2009, MNRAS, 394, 1956
Cross N., Driver S. P., 2002, MNRAS, 329, 579
Davis M., Huchra J., 1982, ApJ, 254, 437
Driver S. P., 1999, ApJ, 526, L69
Driver S. P., Popescu C. C., Tuffs R. J., Liske J., Graham A. W., Allen P. D., de Propris R., 2007, MNRAS, 379, 1022
Driver S. P. et al., 2009, Astron. Geophys., 50, 5.12
Driver S. P. et al., 2011, MNRAS, 413, 971
Eales S., 1993, ApJ, 404, 51
Efstathiou G., Ellis R. S., Peterson B. A., 1988, MNRAS, 232, 431
Ellis S. C., Bland-Hawthorn J., 2007, MNRAS, 377, 815
Ellis R. S., Colless M., Broadhurst T., Heyl J., Glazebrook K., 1996, MNRAS, 280, 235

Faber S. M. et al., 2007, ApJ, 665, 265
Folkes S. R. et al., 1999, MNRAS, 308, 459
Geller M. J., Diaferio A., Kurtz M. J., Dell'Antonio I. P., Fabricant D. G., 2011, AJ, submitted
Graham A. W., Driver S. P., Petrosian V., Conselice C. J., Bershady M. A., Crawford S. M., Goto T., 2005, AJ, 130, 1535
Hill D. T., Driver S. P., Cameron E., Cross N., Liske J., Robotham A., 2010, MNRAS, 404, 1215
Hill D. T. et al., 2011, MNRAS, 412, 765
Hopkins A. M., 2004, ApJ, 615, 209
Hopkins A. M., Beacom J. F., 2006, ApJ, 651, 142
Humason M. L., Mayall N. U., Sandage A. R., 1956, AJ, 61, 97
Ilbert O. et al., 2005, MNRAS, 439, 863
Jones D. H., Peterson B. A., Colless M., Saunders W., 2006, MNRAS, 369, 25
Kharchenko N. V., Scholz R.-D., Piskunov A. E., Roeser S., Schilbach E., 2007, Astron. Nachr., 328, 889
Kistler M. D., Yuksel H., Beacom J. F., Hopkins A. M., Wyithe J. S. B., 2009, ApJ, 705, L104
Lawrence A. et al., 2007, MNRAS, 379, 1599
Lilly S. J., Le Fevre O., Hammer F., Crampton D., 1996, ApJ, 460, L1
Lin H., Yee H. K. C., Carlberg R. G., Morris S. L., Sawicki M., Patton D. R., Wirth G., Shepherd C. W., 1999, ApJ, 518, 533
Lineweaver C. H., Tenorio L., Smoot G. F., Keegstra P., Banday A. J., Lubin P., 1996, ApJ, 470, 38
Liske J., Lemon D. J., Driver S. P., Cross N. J. G., Couch W. J., 2003, MNRAS, 344, 307
Liu C., Capak P., Mobasher B., Paglione T. A. D., Rich R. M., Scoville N. Z., Tribiano S. M., Tyson N. D., 2008, ApJ, 672, 198
Lotz J. M., Jonsson P., Cox T. J., Croton D., Primack J. R., Somerville R. S., Stewart K., 2011, ApJ, preprint (arXiv:1108.2508v1)
Loveday J., 1997, ApJ, 489, 29
Loveday J., 2000, MNRAS, 312, 557
Loveday J., 2004, MNRAS, 347, 601
Montero-Dorta A. D., Prada F., 2009, MNRAS, 399, 1106
Noeske K. G. et al., 2007, ApJ, 660, L47
Norberg P. et al., 2002, MNRAS, 336, 907
Peng Y.-J. et al., 2010, ApJ, 721, 193
Prescott M., Baldry I. K., James P. A., 2009, MNRAS, 397, 90
Sandage A., Tammann G. A., Yahil A., 1979, ApJ, 232, 352
Saunders W., Cannon R., Sutherland W., 2004, Anglo-Australian Obs. Newsl., No. 106, 16
Schechter P. L., 1976, ApJ, 203, 297
Schlegel D. J., Finkbeiner D. P., Davis M., 1998, ApJ, 500, 525
Schmidt M., 1968, ApJ, 151, 393
Smith A. J., Loveday J., Cross N. J. G., 2009, MNRAS, 397, 868
Soneira R. M., Peebles P. J. E., 1978, AJ, 83, 845
Strateva I. et al., 2001, AJ, 122, 1861
Tonry J. L., Blakeslee J. P., Ajhar E. A., Dressler A., 2000, ApJ, 530, 625
Trentham N., Tully R. B., 2002, MNRAS, 335, 712
Willmer C. N. A. et al., 2006, ApJ, 647, 853
York D. G. et al., 2000, AJ, 120, 1579
Yuksel H., Kistler M. D., Beacom J. F., Hopkins A. M., 2008, ApJ, 683, 5
Zehavi I. et al., 2005, ApJ, 630, 1
Zehavi I. et al., 2011, ApJ, 736, 59
Zucca E. et al., 2009, A&A, 508, 1217

APPENDIX A: TESTING THE METHODS

We here test our methods using simulated mock catalogues. We generate clustered distributions of points with known evolving LF and then apply the GAMA selection effects to create a set of mock catalogues.

A1 Clustered simulations

We use a Soneira & Peebles (1978) type simulation to generate a clustered distribution of points in a cube 1200 h^{-1} Mpc on a side

Table A1. LF parameters estimated from both non-evolving and evolving simulated data. The recovered values show the mean and standard deviation from eight mock catalogues.

	α	$M^* - 5 \log h$	$\phi^*/h^3 \, \mathrm{Mpc}^{-3}$	Q	P
True	-1.20	-20.80	0.0100	0.00	0.00
Recovered	-1.19 ± 0.01	-20.78 ± 0.02	0.0101 ± 0.0007	0.04 ± 0.06	-0.03 ± 0.30
True	-1.20	-20.80	0.0100	2.00	0.00
Recovered	-1.20 ± 0.01	-20.79 ± 0.02	0.0101 ± 0.0004	2.05 ± 0.05	-0.07 ± 0.13

with periodic boundary conditions. The parameters in the simulation are chosen to yield similar clustering properties to those measured by Zehavi et al. (2005) for a flux-limited sample of SDSS galaxies, namely a correlation function with power-law slope $\gamma \simeq 1.7$ and correlation length $r_0 \simeq 5.2 \, h^{-1}$ Mpc. This allows us to investigate the effects of large-scale structure on our LF estimates.

With the observer located at one corner of the cube, each galaxy in the simulation was assigned an absolute magnitude M within the range $-24 \leq M_r \leq -10$ mag, drawn at random from a LF with parameters specified in Table A1. Since these are static simulations, we assume a linear redshift–distance relation, with $r = cz/H_0$ and volume element $dV \propto r^2$. Apparent magnitudes m are calculated using $m = M + 25 + 5 \log r (1 + z)$ with no K-correction. Strictly, of course, there is no factor $(1 + z)$ in luminosity distance in Euclidean space. We choose, however, to include this factor in the simulations to make them more realistic – without it one predicts far too many galaxies at higher redshifts. The number of observable galaxies N_{obs} to redshift $z_{\mathrm{max}} = 0.4$ in each simulation cube was determined by integrating the model LF $\phi(L, z)$ over luminosity and redshift:

$$N_{\mathrm{obs}} = \int_0^{z_{\mathrm{max}}} \int_{L_{\mathrm{min}}(z, m_{\mathrm{lim}})}^{\infty} \phi(L, z) dL \frac{dV}{dz} dz, \qquad (A1)$$

with $m_{\mathrm{lim}} = 19.8$ mag.

We crudely mimic the GAMA survey geometry by selecting galaxies within each of three $12 \times 4 \, \mathrm{deg}^2$ regions (bounded by latitude $0° < \phi < 4°$ and longitudes $0° < \theta < 12°$, $36° < \theta < 48°$ and $78° < \theta < 90°$).

Imaging completeness is determined by linear interpolation of the curve in Fig. 1. r-band half-light surface brightness, $\mu_{50,r}$, for each simulated galaxy is assigned according to the empirically observed relation between $\mu_{50,r}$ and r-band absolute magnitude $^{0.1}M_r$ for GAMA galaxies, $\mu_{50,r} = 22.42 + 0.029 \, ^{0.1}M_r$ with 1σ scatter of 0.76 mag. Target completeness is obtained using the empirically observed completeness shown in Fig. 2. Note that we do not attempt to follow the dependence of target completeness on sky coordinates, and so therefore any dependence of target completeness on target density in the real data will not be simulated. Given the better than 98 per cent completeness of GAMA spectroscopy, this should not be a significant issue. Finally, spectroscopic completeness is obtained by generating a fibre magnitude for each simulated galaxy according to the empirically observed relation between Petrosian and fibre magnitudes for GAMA galaxies, $r_{\mathrm{fib}} = 5.84 + 0.747 r_{\mathrm{Petro}}$ with 1σ scatter of 0.31 mag. Redshift completeness is then obtained using the sigmoid function fit to redshift success shown in Fig. 3.

Considering each form of completeness in turn, galaxies are selected at random with a probability equal to the completeness. Weights for the simulated galaxies that survive this culling process are assigned in the same way as for observed galaxies (equation 2).

A2 Simulation results

Eight independent mock catalogues were generated for each of two different input LFs, as described above, and used as input catalogues for our LF estimation code. Naturally, when analysing
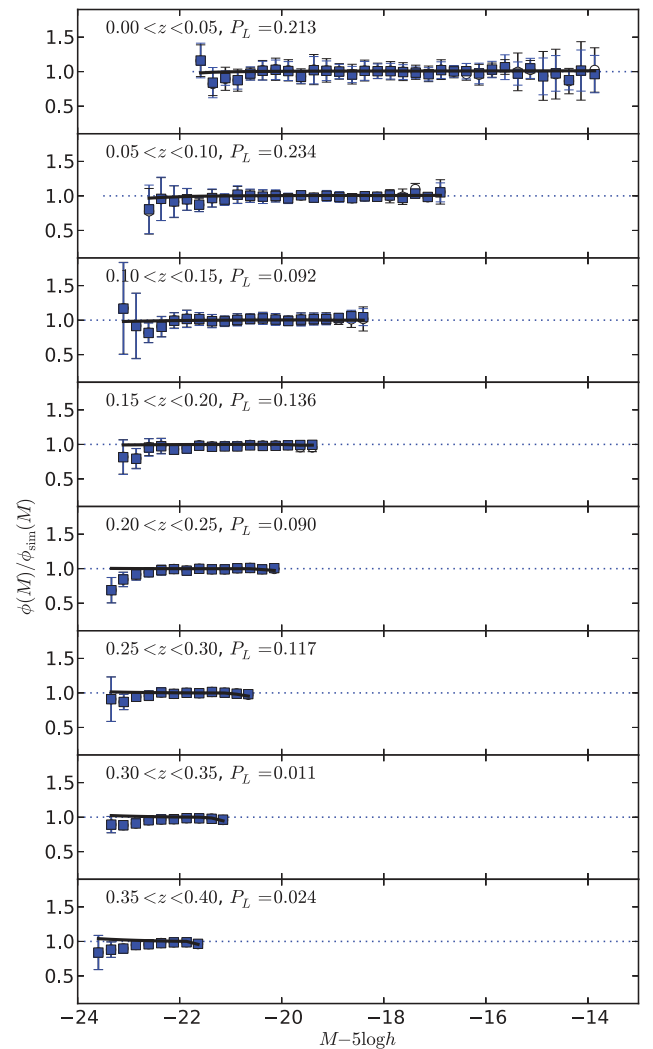

Figure A1. Simulated evolving LF estimates in eight redshift slices as indicated. All estimates have been normalized by the 'true' underlying LF of the evolving simulations; a perfect estimate would like along the horizontal dotted line. The open symbols show the mean from eight mock catalogues determined using the $1/V_{\mathrm{max}}$ estimator; the filled symbols are from the SWML estimator. The error bars for each come from the scatter between the eight mocks. The continuous lines show the best-fitting evolving parametric fit, as given by equation (21). P_L gives the likelihood ratio determination of how well the parametric fit describes the SWML observations in that range.
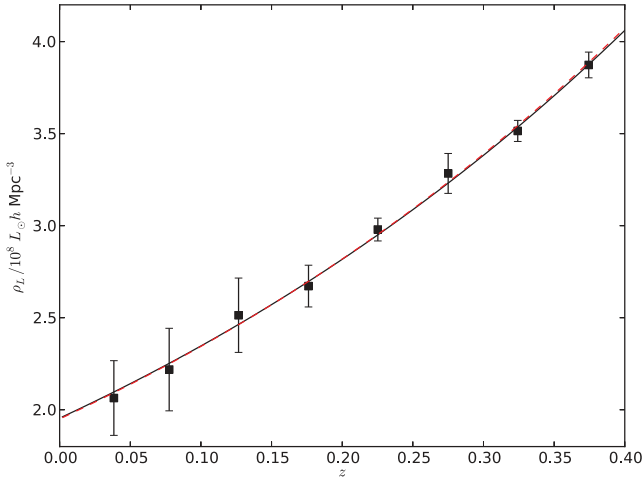
Figure A2. Luminosity density estimated from simulated data in eight redshift slices. The symbols with error bars show the mean and rms from eight mock catalogues determined using equation (16). The continuous line shows the mean parametric prediction of LD evolution (equation 14) and the red dashed line shows the expected evolution, given the simulation parameters.

these simulations, we assume a consistent cosmology in calculating distances, apparent magnitudes and volumes.

The Schechter function parameters recovered by the parametric LF estimator, for both non-evolving and pure luminosity evolution simulations, are given in Table A1. In both cases, we recover the true LF parameters with minimal bias, $\sim 1\sigma$ at worst.

Fig. A1 shows the LF recovered in eight redshift slices from our evolving mock catalogues. In order to amplify any discrepancies, all estimates have been normalized by the true LF, obtained by substituting the input LF parameters into equation (21). We only plot binned estimates when there is at least one galaxy in that magnitude bin in all eight realizations in order to avoid biasing the mean high if only realizations with one or more galaxies are included or biasing

it low if all realizations are used. This eliminates bins fainter than $M = -13$ mag, for which galaxies are only found in a subset of the simulations.

For the low-redshift ($z < 0.05$) slice, all estimates are in good agreement with the true LF. Faintwards of $M_r \simeq -16$ mag, the scatter in $1/V_{\max}$ estimates starts to increase due to density variations induced by large-scale structure. The SWML estimator, being insensitive to density variations, has smaller error bars at the faint end.

For the higher redshift slices, we see that $1/V_{\max}$ and SWML estimators give essentially identical results. There is a tendency for both of these binned estimates to slightly underestimate the bright end of the LF, a consequence of the fact that both binned estimates, unlike our parametric fit, make the assumption that the LF is independent of redshift. Even dividing the simulation into eight redshift slices of width $\Delta z = 0.05$, there is a systematic change of $\Delta M^* = 0.1$ across each slice in these $Q = 2$ simulations. With broader redshift slices, the discrepancy worsens. For example, with $\Delta z = 0.1$, the likelihood ratio probabilities are below 0.001 for the three higher redshift slices. It is likely that our binned estimates of the GAMA LF (Section 4) are biased in a similar fashion. Note that Cole (2011) has recently proposed a method for estimating binned LFs whilst simultaneously fitting for luminosity and density evolution.

Fig. A2 shows the LD estimated from the evolving simulations. The recovered LD, both in redshift bins, equation (16), and as predicted by the parametric fit, equation (14), is in excellent agreement with the prediction, given the simulation parameters. The decreasing errors at higher redshift indicate that sample variance is the largest contributing factor to errors in LD for these simulations. This is not the case with the observed LD (Section 4.5), where the dominant source of error, particularly for the u and g bands, is the applicability of the evolution model (equation 5).

This paper has been typeset from a TEX/LATEX file prepared by the author.